Mon. Not. R. Astron. Soc. **288,** 19–42 (1997)

On the polarization of resonantly scattered emission lines – III. Polarization of quasar broad emission lines and broad absorption line troughs

H.-W. Lee and R. D. Blandford

Department of Theoretical Astrophysics, California Institute of Technology, Pasadena, CA 91125, USA

Accepted 1997 January 3. Received 1996 May 24; in original form 1995 September 25

ABSTRACT

The contribution to the expected linear polarization of quasar broad emission and absorption lines from resonance scattering is computed using a Monte Carlo approach for specific, generic models. Attention is focused on the external illumination of the scattering region. The polarization of the reflected component from an externally illuminated slab with finite optical depth is first considered as a model of a single, dense, broad emission-line cloud. A polarization $\lesssim 40$ per cent ($\lesssim 10$ per cent) is typically computed for $J=0\rightarrow 1$ ($J=1/2\rightarrow 3/2$) transitions. Integration over a population of emission-line clouds typically reduces the observed polarization by a factor $\sim(0.1\text{–}0.3)q_{\rm BELR}$, where $q_{\rm BELR}$ is the covering factor for emission lines, while preserving the relative polarizations of different lines. Consequently, the low degree of polarization observed in the red wings of quasar emission lines limits the density of low column density emission-line clouds.

Broad absorption lines are associated with outflowing gas of lower density. The polarization of both the transmitted and the reflected radiation is next computed for simple kinematic models of the outflow and the observed integrated polarization in the absorption-line troughs is found to be typically ~ 10 per cent. An equatorial flow model gives a large degree of polarization (~ 0.15) parallel to the symmetry axis in the absorption trough for the doublet transition $J=1/2\rightarrow 1/2, 3/2$, and the polarized flux is found to extend to the red side. In contrast, we obtain a smaller degree of polarization (~ 0.05) perpendicular to the jet axis from a bipolar flow model and the polarized flux is concentrated to the blue side of the line profile. It is predicted that the troughs of singlet $J=0\rightarrow 1$ lines, such as C III $\lambda 977$, should exhibit larger degrees of polarization if this is due to resonance scattering. Polarization observations of quasar emission lines promise to be a powerful diagnostic of the kinematics of gas in the central pc of a quasar.

Key words: polarization – galaxies: kinematics and dynamics – quasars: absorption lines – quasars: emission lines.

1 INTRODUCTION

A distinctive and defining property of many active galactic nuclei (AGN) is the presence of broad emission lines (BELs). Quasars and type 1 Seyfert galaxies typically exhibit lines with widths in excess of ~ 1000 km s^{-1} (e.g. Osterbrock 1989). In addition, roughly 10 per cent of radio-quiet quasars exhibit broad, blueshifted, absorption-line troughs (e.g. Weymann et al. 1985). Although the kinematic details remain controversial, these observations are widely interpreted in terms of a model in which a central UV continuum source is surrounded by a broad-line region containing dense clouds moving with large speeds from which emanates an outflow of more tenuous gas (at least in the case of the radio-quiet quasars).

Spectropolarimetry has already contributed much to our understanding of AGN. In particular, Antonucci & Miller (1985) showed that Seyfert 2 galaxies sometimes show

broad-line components in their polarized spectra and argued that they were similar to Seyfert 1 galaxies except that their broad emission-line regions are occulted by a thick molecular torus at low latitude and scattered by electrons at high latitude (e.g. Miller & Goodrich 1990). Polarization can also be created by dust, via transmission and reflection, and through scattering by the resonant ions themselves. The central regions of AGN are manifestly anisotropic, and so it is to be expected that scattering generally produces polarization in AGN spectra. To date, polarization observations of AGN spectra have been limited to the brightest objects, but the advent of 10-m class telecopes and more sensitive polarimeters should increase their role as diagnostics.

Lee, Blandford & Western (1994, Paper I) introduce a formalism for computing the polarization of resonantly scattered emission lines and Lee (1994, Paper II), used a Monte Carlo code to compute the polarization to be expected from a population of non-spherical and anisotropically expanding emission-line clouds. It was found that standard emission-line clouds emit almost unpolarized line radiation except when they have optical depths $\tau \sim 1$ as may be the case for the semiforbidden C III] λ1909 transition.

In this paper, we address the possibility that photons are polarized by resonance-line scattering after they have left their emission sites. We attempt to make semi-quantitative statements about the expected degree and direction of the polarization of quasar lines. We do this in the context of some fairly general, geometrical and radiative assumptions about the emitting and scattering gas, which we introduce in Section 2. In Section 3, we compute the polarization to be expected from scattering within the emission-line region. We first perform Monte Carlo simulations of scattering by a single, stationary cloud and then estimate the integrated polarization from a large population of clouds. We next turn to broad absorption line (BAL) quasars (BALQs). The line photons that appear to be 'absorbed' are actually scattered by anisotropically distributed, outflowing gas with modest line optical depths. We compute the magnitude of the resulting polarization in some simple kinematic models of the outflow using a hybrid Sobolev–Monte Carlo method in Section 4. Global models are presented in Section 5. Finally, inferences that can be drawn from existing polarization observations of AGN and the promise of future observations are discussed in Section 6.

2 GENERIC QUASAR MODEL

2.1 Emission-line region

We suppose, in common with many models (e.g. Netzer 1990), that there is a compact, central continuum source of unpolarized ionizing radiation of size $\lesssim 10^{16}$ cm, surrounded by a zone, of size $R_{\rm BELR} \lesssim 1$ pc, in which are found dense, line-emitting clouds [with electron density $n_{\rm e} \sim 10^{8}$–10^{10} cm^{-3} and temperature $T \sim (1$–$3) \times 10^{4}$ K]. We further suppose that this gas has a small filling factor $f \sim 10^{-6} (R_{\rm BELR}/1\ {\rm pc})^{-2}$, a modest broad emission-line region (BELR) covering factor $q_{\rm BELR} \sim 0.1$, and an ionization parameter $U \equiv n_{\rm UV}/n_{\rm e} \sim 0.1$–$1$. The velocity distribution of the clouds within this zone determines the line profiles, and the clouds may well be stratified so that ions with different ionization potentials are concentrated at different distances from the central continuum source (e.g. Peterson et al. 1990). In addition, we suppose that there is an opaque disc/torus which prevents an observer from seeing the emission lines from an equatorial direction as well as from the other hemisphere.

For present purposes, we need only suppose that individual clouds may be modelled as discrete regions that are individually optically thick to the permitted resonance-line photons of primary interest to us. In standard cloud models, the hydrogen column densities are supposed to be $N_{\rm H} \sim 10^{22}$–10^{23} cm^{-2}, at least five orders of magnitude larger than the minimum column density needed to be optically thick to most of the prominent emission lines (except the C III] λ1909 semi-forbidden line). The connectivity and confinement of these clouds is problematic. One possibility (Rees 1987; Emmering, Blandford & Shlossman 1992, henceforth EBS), is that both the confinement and acceleration be attributable to the action of a strong magnetic field. The origin of the emission gas is not especially relevant here, although accretion discs (e.g. EBS), giant stars (e.g. Scoville & Norman 1995) and supernovae (e.g. Perry & Dyson 1985; Williams & Perry 1994) have all been considered.

Of great importance for determining the polarization is the velocity distribution of these clouds. It is observed that quasar line profiles are centrally peaked with velocity widths $\Delta V_{\rm em} \sim 10\,000$ km s^{-1}. This is generally supposed to represent space motion of the emitting gas (although electron scattering may contribute to the wings of the lines: Weymann 1970; EBS). In some quasars, the high-ionization lines (HILs) are blueshifted with respect to the low-ionization lines (LILs), and some broad lines have blue asymmetry (e.g. Peterson et al. 1991, 1994; Corbin & Francis 1994). This is roughly consistent with an accretion disc model in which a wind accelerates away from a disc. We shall adopt this interpretation for illustrative purposes and use it to bring out some features of line formation in the polarized flux.

2.2 Formation of broad absorption lines

The troughs in BALQs are observed in highly ionized, permitted lines and their velocity widths range up to $\sim 0.1c$, although a fraction exhibit lower ionization broad Mg II absorption. The absorption-line profiles are reminiscent of those formed in the spectra of P Cygni stars, which also suggests that the absorption region is dominated by outflow. Many troughs are 'detached' in velocity from their associated emission lines with steep walls at their low-velocity ends. This indicates that the kinematics is more complex than the simple radial outflow associated with models of P Cygni stars. In particular, it suggests that the variation of the radial velocity of the absorbing gas along the line of sight is non-monotonic and exhibits a minimum.

Weymann et al. (1991) showed that the emission-line properties of BALQs are almost identical to those of non-BALQs, and developed a model in which all radio-quiet quasars have outflowing BAL clouds confined to an equatorial fan of total angular width $\sim 20°$. A total column density of outflowing gas $\gtrsim 3 \times 10^{20}$ cm^{-2} is needed (assuming solar abundances). This is perhaps a few per cent of the mean column density associated with the BELR. The filling

factor of the absorbing gas is generally assumed to be small for similar reasons to those given for emission lines. The confinement of the absorbing clouds is also problematic. Again, a magnetic field provides a possible mechanism for achieving this.

Absorption troughs have velocity widths that are typically 3 times broader than the emission lines, which implies that the absorbing gas is accelerated from rest. It may be drawn from emission-line gas (e.g. Murray, Grossman & Chiang 1995), from giant stars in a central cluster (e.g. Scoville & Norman 1995) or from the surface of an orbiting accretion disc (e.g. Weymann et al. 1982; EBS; Murray et al. 1995). This last possibility implies that the gas will start from zero latitude with the local Keplerian velocity without completely occulting the BELR, as there is no absorption at zero velocity. As the outflowing gas expands away from the disc plane, it will eventually reach the latitude of the observer and occult the BELR and the continuum. The gas that does this first will presumably have high speed, as it originates at small radius. The ray from the observer may then pass through more slowly moving gas, on a different streamline, before finally encountering the gas that has been strongly accelerated. This is one way by which a minimum may be formed in the velocity of the outflow.

Most of the broad absorption troughs are not completely black. It is unreasonable to assume that the column density and ion abundances are adjusted so that the optical depth always saturates at $\tau \sim 2$. We suppose that photons are removed from the beam along the direct line of sight from the continuum source, either partially or effectively totally, dependent upon velocity, and that there is a scattering from other lines of sight which partially refills the troughs at a level $\lesssim 0.1$ of the continuum flux dependent upon the total covering fraction and velocity of the BAL (cf. Turnshek et al. 1988, Hamann, Korista & Morris 1993). BALQ variability (Barlow et al. 1992 and references therein) is apparently common on time-scales of weeks to months, and is consistent with this interpretation.

The smoothness of BAL profiles on a velocity scale ranging from values comparable with the thermal width of the absorbing gas to those $\sim 10\,000$ km s^{-1} (Barlow & Junkkarinen, in preparation) indicates that the absorbing gas either flows smoothly (cf. Murray et al. 1995) or is contained in a spray of small clouds (e.g. Weymann et al. 1992; Arav, Li & Begelman 1994). (Scattering into other lines of sight can also smooth the profiles). As a consequence, no detailed model of the broad absorption line region (BALR) is necessary to explore the polarization beyond a rough specification of the disposition of the gas in phase-space.

2.3 Polarization mechanisms

There are many possibilities for creating polarization in the observed line and continuum emisson. First, as discussed in Paper II, individual dense clouds whose ions create line photons following recombination or collisional excitation may be polarizing if they are non-spherical in shape or have an anisotropic velocity gradient tensor. The observed polarization depends upon the global average of these properties over the ensemble of clouds. Typically, this contribution to the polarization is unobservably small for permitted lines, because the scattering optical depth of an individual cloud is so large.

Secondly, polarization may be produced by reflection of resonance-line photons. This arises when either an emission-line photon produced in an emission-line cloud or a continuum photon created in the central continuum source is incident upon an element of gas moving with a bulk velocity that Dopper shifts the photon into resonance with a permitted transition. The column density of gas necessary to produce a single reflection is typically $\sim 10^{17}$ cm^{-2} for the most prominent UV permitted lines (cf. Paper I). This gas may be found in the emission-line regions or in the more tenuous, higher velocity gas associated with the BALR. Reflection of resonance-line radiation produces a polarization perpendicular to the scattering plane with a degree that depends upon the scattering angle, in a manner similar to Thomson scattering, being large for a $\pi/2$ scattering and small for forward or backward scattering. The degree of polarization is reduced from that associated with single Thomson scattering on account of multiple scattering and it also depends upon the electronic transition involved. The total degree of polarization obtained by combining the transmitted and the reflected radiation is dictated by the spatial distribution of scatterers and is likely to be frequency dependent across the line.

Thirdly, there may be a broad-band polarizer present affecting both the lines and the continuum. One possibility is scattering by dust (e.g. Laor & Draine 1993). This will create a wavelength-dependent degree of polarization. In addition, polarization can be created in transmission if there is an organized magnetic field present along the line of sight. In this case, however, an appreciable fraction of the photons that are removed from a beam are not absorbed by the grains but are scattered and, unlike the case of interstellar polarization, photons scattered into our line of sight from other beams must be included in the overall polarization. The other common type of broad-band polarizer is electron scattering, where the polarization should be frequency independent (e.g. Antonucci & Miller 1985; Tran, Miller & Kay 1992; Goodrich & Miller 1994), and where, as with resonance-line reflection, the largest polarization is produced when the scattering angle is $\sim \pi/2$. However, this requires that there be a column density of ionized gas $\gtrsim 10^{23}$ cm^{-2}.

3 POLARIZATION FROM THE EMISSION-LINE REGION

3.1 Reflected polarization from a single cloud

In Paper II, we developed a Monte Carlo code to compute the polarization of resonantly scattered photons originating within an anisotropically expanding cloud. The same code is used now to compute the polarization of resonantly scattered radiation originating outside the cloud and reflected by it. In this case, some photons are only scattered once and these can be highly polarized. However, other photons are multiply scattered and this usually lowers the overall degree of polarization. In addition, some photons may penetrate the cloud and be transmitted.

We model the cloud as a plane slab of infinite extent in the x and y directions and of finite optical depth τ in the z

direction. For the moment, we work in the rest frame of the slab and ignore velocity gradients. The polarization decreases as the optical depth τ of the slab increases, and at $\tau \sim 10$ the polarization reaches the saturation value. The largest polarization arises when the ground state angular momentum quantum number is 0, as discussed in Papers I and II.

In Fig. 1 we show the result of computing the polarization of the emergent light scattered from a slab with $\tau = 5$, where the slab is illuminated by an unpolarized source. We introduce spherical polar coordinates θ, ϕ and allow the incident photons to propagate along a direction (θ_{in}, ϕ_{in}) and be scattered into the $(\theta_{out}, \phi_{out})$ direction. The scattering angle is $\alpha = \cos^{-1}[\cos\theta_{in}\cos\theta_{out} + \sin\theta_{in}\sin\theta_{out}\cos(\phi_{in} - \phi_{out})]$ and the direction of polarization is perpendicular to the scattering plane. The transition is $J = 0 \rightarrow 1$ (e.g. C III λ977, Al III λ1671). The polarization is most dependent on α, but varies slowly for $\mu_{out} \gtrsim 0.5$. The highest polarization (~ 0.5) is attained when $\alpha \sim \pi/2$. The polarization for the transition $J = 1/2 \rightarrow 3/2$ is displayed in Fig. 2. Most of the prominent AGN emission lines (including C IV λ1549, Si IV λ1397, Mg II λ2798, N V λ1240, O VI λ1031) are doublets with the higher frequency component having weight 2/3 and corresponding to a $J = 1/2 \rightarrow 3/2$ transition and the lower frequency component corresponding to $J = 1/2 \rightarrow 1/2$ with weight 1/3. The velocity separations of these doublets range from ~ 500 km s^{-1} for C IV to ~ 2600 km s^{-1} for Si IV. These splittings are conveniently large compared with the thermal velocities within individual clouds, but are small compared with total line velocity widths. As explained in Paper I, when photons are resonant with the $J = 1/2 \rightarrow 1/2$ transition, the scattered polarization is zero, independent of the incident polarization. Therefore we can average the polarization over the doublet by multiplying the result for a $J = 1/2 \rightarrow 3/2$ simulation by 2/3. We find that the polarization behaviour for $J = 1/2 \leftarrow 3/2$ is almost identical to the case of the transition $J = 0 \rightarrow 1$, except that the overall degree of polarization is reduced by a factor of ~ 0.4. This is similar to the ratio for a single scattering through an angle $\pi/2$, as shown in Paper I, and for the integrated polarization from a stationary ellipsoidal cloud, as shown in Paper II. Therefore the net reflection polarization expected for scattering by a single cloud for a $J = 1/2 \rightarrow 1/2$, 3/2 doublet transition such as C IV λ1549 is expected to be ~ 30 per cent of the value for a $J = 0 \rightarrow 1$ singlet case such as C III λ977.

We also consider the dependence on the azimuthal angle between the source and the observer, fixing the position of the scatterer. In the left panel of Fig. 2, the numerical result is shown by various points with error bars with $\mu = \frac{1}{2}$(fixed) and ϕ_{out} takes the values of 0, $\pi/4$, $\pi/2$, $3\pi/4$ and π. The theoretical maximum polarization (i.e. single electron scattering) is plotted for comparison with the case of the transition $J = 0 \rightarrow 1$. In the right panel the polarization from the transition $J = 1/2 \rightarrow 3/2$ is shown. The degree of polarization remains at about 40 per cent of the value for $J = 0 \rightarrow 1$. Note that the scale is different and the polarization should be

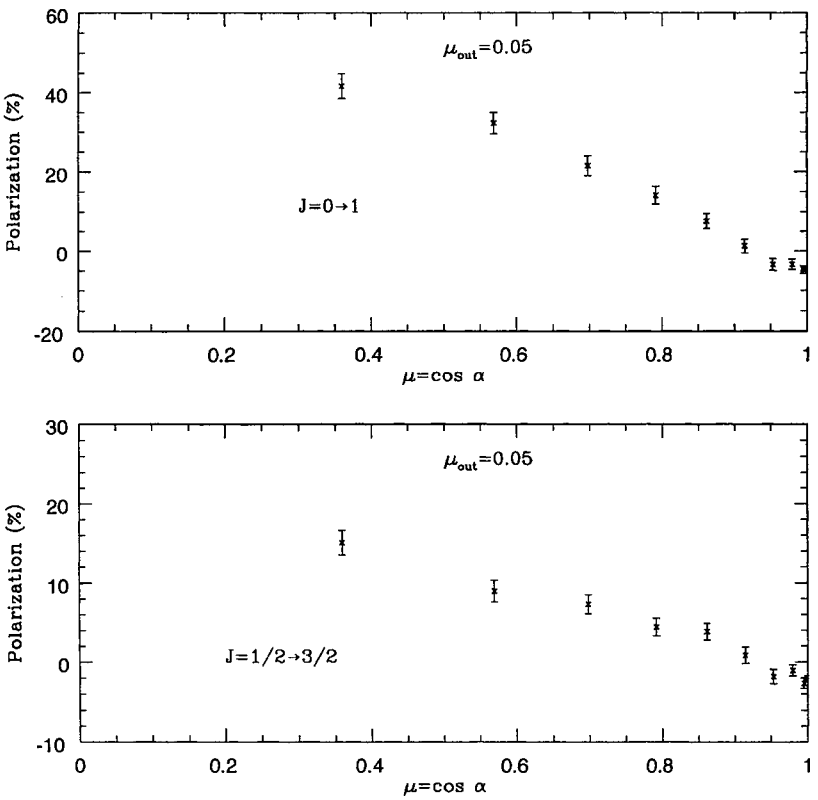

Figure 1. Polarization of the emergent light from an illuminated slab with optical depth $\tau = 5$, when the source and the observer are collinear. In the upper panel the polarization for transition $J = 0 \rightarrow 1$ is shown. In the lower panel the polarization for transition $J = 1/2 \rightarrow 3/2$ is shown. Note that for the doublet transition $J = 1/2 \rightarrow 1/2$, 3/2 a multiplicative statistical factor of 2/3 should be included in order to obtain the correct degree of polarization. The horizontal axis represents the cosine of the scattering angle α defined in the text. The photons scattered into $\mu_{out} \leq 0.1$ are collected from various incident directions.

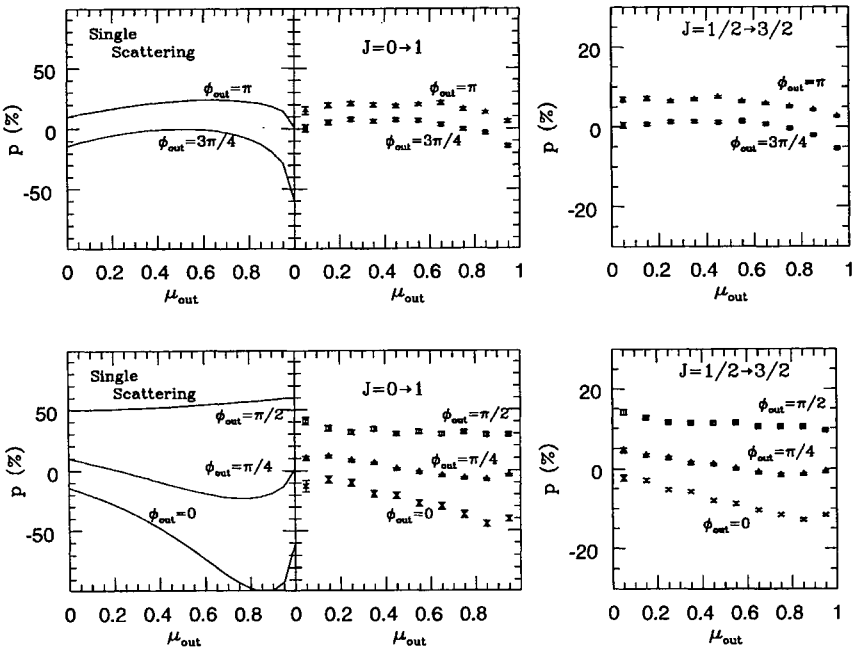

Figure 2. Polarization of the emergent light from an illuminated slab with optical depth $\tau=5$, where the source and the observer are not collinear. The light source is fixed in the direction of $\mu=0.5$, $\phi=0$ and the scattered photons are collected as a function of $\mu_{out}=\cos\theta_{out}$ for different azimuthal angles. The continuous lines represent the result from single scattering which generally gives the largest degree of polarization. In the left panels the transition is $J=0\rightarrow1$ and in the right panels the result is for the transition $J=1/2\rightarrow3/2$. In order to obtain the result for the doublet transition $J=1/2\rightarrow1/2$, 3/2, the statistical factor 2/3 should be included (cf. Fig. 1).

further reduced by a factor of 2/3 for the case of the doublet transition $J=1/2\rightarrow1/2$, 3/2. Again the largest polarization is seen when the scattering angle is 90°. When $\phi_{in}\sim\phi_{out}$, the electric vector lies in the slab. Moreover when $|\phi_{in}-\phi_{out}|\sim\pi/2$, the polarization direction is roughly perpendicular to the slab.

3.2 Polarization from reflection by a population of emission-line clouds

We next consider the scattering of unpolarized light incident upon an ensemble of emission-line clouds and compute the observed polarization. For illustration, we adopt a particular, idealized, kinematic model in which the clouds are illuminated by a central continuum source and there is an optically thick accretion disc present, so that only the hemisphere nearer to the observer can be seen (cf. EBS). We assume that there is axial symmetry. The velocity of each cloud is assumed to be purely poloidal, making an angle θ_i with the disc, and to vary with distance from the central source in proportion to $r^{-1/2}$ over three decades of radius. We assume that the number density $n(r)$ of clouds is proportional to r^p, where $p\sim-1.5$. The optical depth of each cloud is taken to have a constant value τ for a resonant photon at line centre. Hence the frequency of the emergent photons is determined by the velocity component of the scattering cloud along the line of sight.

In Fig. 3 we show the polarization, the flux of the scattered component and the polarized flux for $\mu_{out}=0.2$, 0.4, 0.6 and 0.8, respectively, when the clouds are moving along a line inclined at an angle $\theta_i=50°$ to the disc. The horizontal axis represents the observed frequency and the transition is $J=0\rightarrow1$. The degree of polarization of the scattered component is shown to be ~0.35 in the redward wing for $\mu_{out}<0.5$, and double peaks appear for $\mu_{out}>0.5$. Clearly a large polarization is obtained when the incoming and outgoing directions are orthogonal, and this condition is more likely to be met at small values of μ_{out}.

The overall behaviour of the polarization and the polarized flux for the transition $J=1/2\rightarrow3/2$ is almost identical to that of the transition $J=0\rightarrow1$ with the exception that the degree of polarization is reduced by a factor ~0.4. The typical degree of polarization observed in the scattered radiation for this transition is $p\sim0.1$. (Note that for the doublet transition this should be further reduced by a factor of 2/3 again.) However, we should not expect to see this polarization observationally. The success of reverberation mapping (Peterson et al. 1994) indicates that most broad-line photons are not resonantly scattered. In fact if we denote the total covering factor of standard broad-line clouds by q_{BELR}, and the ion thermal velocity by v_{th}, then the observed degree of polarization will be smaller than the degree of polarization in the scattered radiation by a factor $\sim q_{BELR}v_{th}/\Delta V$, and will be negligibly small.

3.3 Influence of small clouds

The clouds that emit most of the line photons may be just the largest representatives of a distribution that extends down to smaller sizes. These clouds probably have similar pressures and temperatures to the standard clouds and consequently similar densities. Although the integral of the hydrogen column density along a line of sight may be dominated by standard, large clouds, the smaller clouds can still be observationally significant if they are spread in velocity and 'fill in' the absorption-line profiles of the prominent

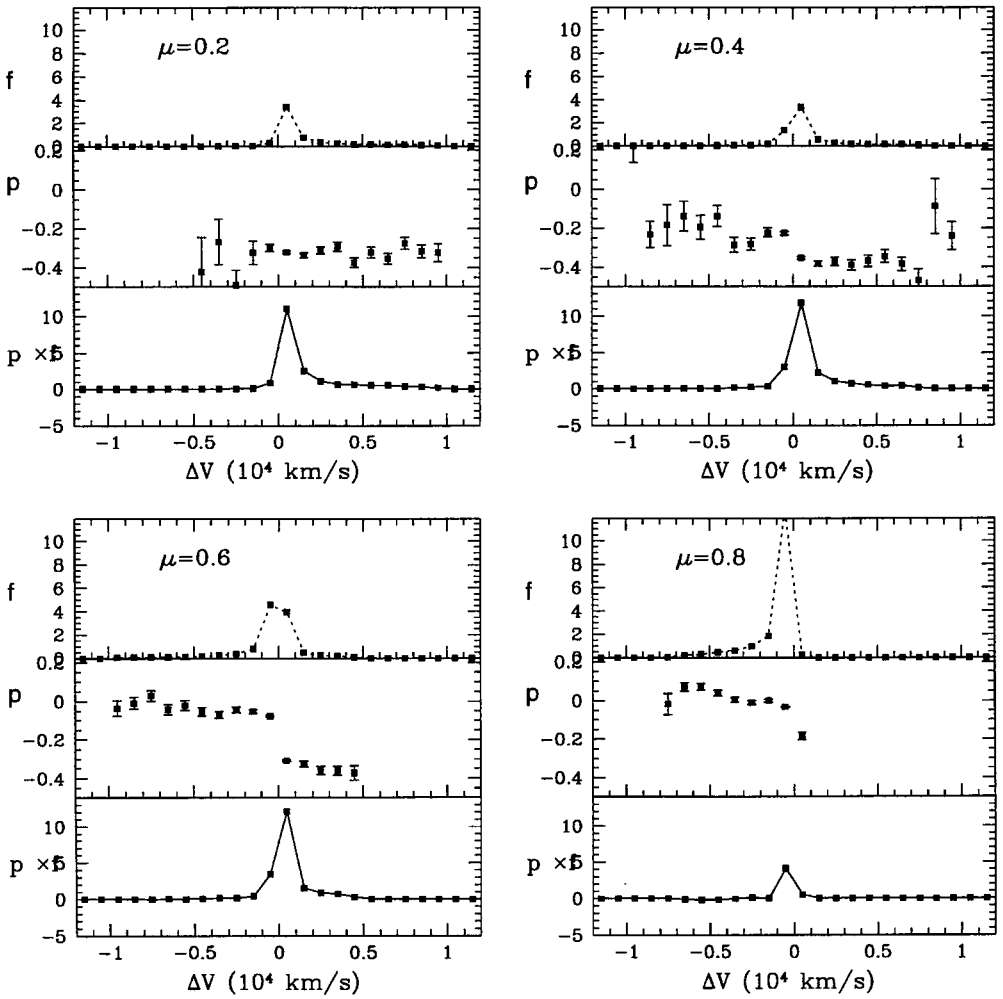

Figure 3. Scattered flux, f, polarization, p, and polarized flux pf of radiation scattered by an ensemble of line-emitting clouds. The continuum source is located at the origin and the clouds are idealized as moving poloidally on straight trajectories originating from the surface of an opaque, equatorial disc. The trajectories make an angle $\theta_i = 50°$ with respect to a radius vector lying in the disc. Azimuthal motion is ignored. The speed of the clouds is assumed to be constant and to scale $\propto r^{-1/2}$, where r is the distance from the origin to the start of the cloud trajectory on the disc surface. The trajectories are supposed to start over a range of three decades of radius so that a range of 30 in observed radial velocity can be accommodated. Individual clouds are observed along directions that make an angle $\cos^{-1}\mu_{\rm out}$ with the symmetry axis.

resonance-line transitions so that $q_{\rm BELR}$ is effectively very large. Just such a phase as this has already been proposed on quite different grounds by Shields, Ferland & Peterson (1995). These hypothetical, small clouds will therefore impede the free escape of emission-line photons and may, as a consequence, impose polarization upon the emission lines by increasing the effective covering factor.

4 POLARIZATION FROM THE ABSORPTION-LINE REGION

4.1 Scattering optical depth

We are interested in the optical depth of an outflow in which the velocity changes montonically with position in such a manner that there is a single point at which an ion moving with the rest frame of the fluid can resonantly absorb photons of a given frequency. Absorption actually occurs within a neighbourhood of this point where the bulk velocity lies within a few thermal widths of its value at resonance. The conventional technique for handling this type of problem is the Sobolev method (e.g. Sobolev 1947; Rybicki & Hummer 1978). This has been applied to problems like line formation and radiative acceleration in O star winds. It is also appropriate to BALQs.

In the presence of a fairly large velocity gradient, all of the absorption at a given frequency occurs over a small region of space within which the physical conditions should be fairly uniform. This is the essence of the Sobolev approximation. The Sobolev optical depth can be written as

$$\tau = n_i \int \sigma \, {\rm d}vc/[v({\rm d}V/{\rm d}s)]$$

$$= n f \lambda \left(\frac{\pi e^2}{m_e c}\right)\left(\frac{{\rm d}V}{{\rm d}s}\right)^{-1} \qquad (4.1)$$

$$\sim 0.3(X_i/10^{-4}) f \lambda_3 ({\rm d}N_{\rm H20}/{\rm d}V_9),$$

where s is the distance along the line of sight, f is the oscillator strength, n_i is the ion density, $X_i = n_i/n_H$ is the abundance of ion i relative to ionized plus neutral hydrogen, $\lambda_3 = \lambda/1000$ Å refers to the emitted wavelength, $dV_9 = d(V/10^9 \text{ cm s}^{-1})$ and $dN_{H20} = n_H\, ds/10^{20}\ \text{cm}^{-2}$ is the differential column density of hydrogen along the line of sight in units of $10^{20}\ \text{s}^{-1}$. Adopting $\tau \sim 1$, $X_i \sim 10^{-4}$ and $f \sim \lambda_3 \sim 1$, we see that the typical column density over which absorption of a given line photon occurs is $\sim 10^{17}\ \text{cm}^{-2}$. However, a total column density of $\gtrsim 3 \times 10^{20}\ \text{cm}^{-2}$ is necessary to absorb throughout the whole absorption trough. These columns are small compared with the column associated with a single, standard emission-line cloud. They are also small compared with the column necessary for significant Thomson scattering ($\sim 10^{24}\ \text{cm}^{-2}$).

4.2 Collisional effects

In Paper I, we distinguished collisional mixing, when the collisions are much more frequent than radiative excitation from the ground state, from radiative mixing, when the reverse is true. (Cf. also Goldreich & Kylafis 1981, 1982, who discussed the radio frequency analogue.) We showed that radiative mixing is obtained when the ionization parameter

$$U = \frac{\int_{\nu_L}^{\infty} d\nu F_\nu/h\nu}{cn_e} \sim \left(\frac{L_{UV}}{10^{46}\ \text{erg}^{-1}}\right)\left(\frac{r}{10^{18}\ \text{cm}}\right)^{-2}\left(\frac{n_e}{10^7\ \text{cm}^{-3}}\right)^{-1} \tag{4.2}$$

satisfies

$$U \gtrsim 0.04\, T_4^{1/2} \nu_{15}^{3/2} f^{-1}, \tag{4.3}$$

where f is the oscillator strength and ν_L is the Lyman limit frequency. This inequality is well satisfied in most models (cf. Hamann et al. 1993). Semiforbidden transitions may, however, be collisionally mixed (cf. Section 5.1).

The rates for collisional excitation are lower by an exponential factor than the rates for collisional mixing of the ground state sublevels. It follows, a fortiori, that we should be able to ignore collisional production of photons in the BAL region and we shall assume this. Furthermore, the excitation time is always short compared with the anticipated dynamical time and so radiative equilibrium can be safely assumed.

4.3 The Sobolev–Monte Carlo approach

The conventional Sobolev approach to line radiative transfer in moving media involves expanding the velocity field to first order about the point of resonance and solving approximately the equations of continuum radiative transfer under the escape probability approximation (e.g. Rybicki & Hummer 1978). Usually this is done without regard to polarization. It is possible to extend this approach to incorporate polarization (e.g. Jeffery 1990 and references therein) but it turns out to be easier and more appropriate for extension to global outflow models to replace the process of solving approximate equations of radiative transfer by a Monte Carlo simulation. We now illustrate the general principles involved by computing the scattered radiation when an unpolarized beam is incident upon some simple flows.

Consider a photon propagating in the direction $\boldsymbol{n}_i$ with frequency $\nu_i = \nu_0 + \Delta\nu$, where ν_0 is the line centre frequency of a given ion after the ith scattering at $\boldsymbol{X}_i$. The Doppler shift $\Delta_i \equiv \Delta\nu/\nu_0$ is given by

$$\Delta_i = \boldsymbol{n}_i \cdot [\boldsymbol{V}(\boldsymbol{X}_i) + \boldsymbol{v}_i]/c, \tag{4.4}$$

where $\boldsymbol{V}(\boldsymbol{X})$ is the velocity field of the flow and $\boldsymbol{v}_i$ is the velocity of the ith scatter relative to the local flow. A distance s along the direction $\boldsymbol{n}_i$ we may approximate the velocity field by

$$\boldsymbol{V}(\boldsymbol{X}_i + s\boldsymbol{n}_i) = \boldsymbol{V}(\boldsymbol{X}_i) + s(\boldsymbol{n}_i \cdot \nabla)\boldsymbol{V}. \tag{4.5}$$

The component of velocity along $\boldsymbol{n}_i$ of the next scatterer must then satisfy

$$\boldsymbol{n}_i \cdot \boldsymbol{v}_{i+1} = \boldsymbol{n}_i \cdot \boldsymbol{v}_i - s\boldsymbol{n}_i \cdot (\boldsymbol{n}_i \cdot \nabla)\boldsymbol{V}, \tag{4.6}$$

and the new Doppler shift is

$$\Delta_{i+1} = \Delta_i + (\boldsymbol{n}_{i+1} - \boldsymbol{n}_i) \cdot [\boldsymbol{V}(\boldsymbol{X}_{i+1}) + \boldsymbol{v}_{i+1}]/c. \tag{4.7}$$

We assume that the 1D velocity $v = \boldsymbol{n} \cdot \boldsymbol{v}$ has a Maxwellian distribution $f_M^1(v) \equiv (1/\sqrt{2\pi}) \exp(-v_2/2)$, where we measure the flow velocity in units of the thermal velocity. As the natural line width is negligible compared with the thermal width, the optical depth τ_{i+1} between the ith and $(i+1)$th scattering is given by

$$\begin{aligned}\tau_{i+1} &= \int_0^{|\boldsymbol{X}_2 - \boldsymbol{X}_1|} ds \int d\boldsymbol{v} f_M^3(\boldsymbol{v})\, \sigma(v) \\ &= \frac{1}{2}\tau_0 \left| \operatorname{erf}(\boldsymbol{n}\cdot\boldsymbol{v}/\sqrt{2}) \right. \\ &\quad \left. - \operatorname{erf}\{[\boldsymbol{n}\cdot\boldsymbol{v} - (\boldsymbol{X}_2 - \boldsymbol{X}_1)\cdot(\boldsymbol{n}\cdot\nabla)\boldsymbol{V}]/\sqrt{2}\} \right|,\end{aligned} \tag{4.8}$$

where $f_M^3(\boldsymbol{v}) \equiv f_M^1(v_x) f_M^1(v_y) f_M^1(v_z)$ is a 3D Maxwellian distribution. Here, τ_0 is given by a generalization of equation (4.1):

$$\tau_0 \equiv n_i f \lambda \left(\frac{\pi e^2}{m_e c}\right) |\boldsymbol{n} \cdot (\boldsymbol{n} \cdot \nabla)\boldsymbol{V}|^{-1}. \tag{4.9}$$

The escape condition is written as $|\boldsymbol{X}_2 - \boldsymbol{X}_1| \to \infty$ and in this case equation (4.9) reduces to

$$\tau_{esc} = \frac{1}{2}\tau_0 \begin{cases} 1 + \operatorname{erf}(\boldsymbol{n}\cdot\boldsymbol{v}/\sqrt{2}) & \text{for } \boldsymbol{n}\cdot(\boldsymbol{n}\cdot\nabla)\boldsymbol{V} > 0 \\ 1 - \operatorname{erf}(\boldsymbol{n}\cdot\boldsymbol{v}/\sqrt{2}) & \text{for } \boldsymbol{n}\cdot(\boldsymbol{n}\cdot\nabla)\boldsymbol{V} < 0. \end{cases} \tag{4.10}$$

The electron collision frequencies are large compared with $|\nabla V|$, and so it is reasonable to assume a Maxwellian ion distribution function. However, this is not a crucial assumption. If there are relatively more highly suprathermal ions in the distribution function, then the photons will have a higher probability of being given a larger Doppler shift. However, there will be a compensatory increase in the opacity at this frequency and the escape probability per scattering will remain at $\sim \tau_0^{-1}$. If, however, there are *no* sufficiently suprathermal ions, so that the photons cannot be Doppler shifted enough to escape directly, then spatial diffusion is inevitably important and our results should be modified.

Since the local thermal speed is small compard with the flow velocity, we can introduce Sobolev surfaces, for a given frequency shift Δ and observer direction $\boldsymbol{n}$ where the flow velocity $\boldsymbol{V}(\boldsymbol{X})$ satisfies $\boldsymbol{n}\cdot\boldsymbol{V}/c=\Delta$. Photons escape from the vicinity of a Sobolev surface by diffusion in frequency rather than in configuration space, and so their last scattering sites are near Sobolev surfaces.

The Sobolev–Monte Carlo procedure then begins by locating the point where the incident photon frequency matches the Doppler shift associated with the bulk velocity. We fix this as the origin of the coordinate system. We next pick a random number $\mathscr{R}$ in $[0,1]$ and assign an optical depth $\tau=-\ln(\mathscr{R})$. If $\tau>\tau_0$, the photon will be transmitted without scattering. Otherwise, we use equation (4.8) to determine the location of the first ($i=1$) scattering as well as the component of ion velocity along $\boldsymbol{n}$. A new propagation direction $\boldsymbol{n}$ and a new polarization direction are generated according to the re-emission probability distribution and the local ion velocity component perpendicular to the previous wavevector is also produced from a 1D Maxwellian distribution (see Paper II) to obtain the new Doppler shift along the new direction using equation (4.7). We then iterate until the photon escapes, noting the emergent direction, the Doppler shift and the polarization.

4.4 Scattering at a singlet Sobolev surface: $J=0\rightarrow1$

We consider first the local problem, that is, scattering at a single Sobolev surface of the unidirectional monochromatic incident radiation field. For the moment, we confine our attention to the simple case of a singlet (S) $J=0\rightarrow1$ for Be-like ions such as C III, N IV and O V, where the polarization pattern is identical to that familiar from classical Thomson scattering.

4.4.1 *Parallel expansion*

We assume that the incident photons propagate along the z-direction which coincides with the only non-zero component of velocity, that is to say $V_z=V_{z0}+zV'$. The Sobolev optical depth along the direction $\boldsymbol{n}=(\sin\theta\cos\phi,\sin\theta\sin\phi,\cos\theta)$ is then given by

$$\tau_{\rm esc}=\tau_0/\cos^2\theta, \tag{4.11}$$

where τ_0 is the optical depth along the z-direction. τ_0 is determined by atomic physics and the local ion density on the Sobolev surface. Note that the optical depth diverges in the perpendicular direction and photons do not escape this way. Observationally, a useful polarization measure is the ratio of the observed polarized flux $F_{\rm P}$ to the total continuum flux $F_{\rm C}$, estimated from measurements at wavelengths where the BALR is transparent. We find that

$$\frac{F_{\rm P}(\nu,\boldsymbol{n})}{F_{\rm C}(\nu,\boldsymbol{n})}=\frac{1}{F_{\rm C}(\nu,\boldsymbol{n})}\int {\rm d}\Omega_{\rm BALR}\,\frac{{\rm d}P}{{\rm d}\Omega}(\nu,\boldsymbol{n}) \tag{4.12}$$

where ${\rm d}\Omega_{\rm BALR}$ is the solid angle subtended by an element of BALR cloud at the continuum source and ${\rm d}\Pi/{\rm d}\Omega$ is the polarized flux scattered per steradian (srad) towards the observer. The polarization ratio $R_{\rm P}=(1/F_{\rm C})({\rm d}P/{\rm d}\Omega)$ can be estimated from the Monte Carlo simulations by the product of the fraction of incident photons scattered per srad and the degree of polarization. As the total solid angle subtended by the BALR is believed to be $\Omega_{\rm BALR}\sim1$ srad, a suitably averaged $R_{\rm P}$ is a measure of the ratio $F_{\rm P}/F_{\rm c}$ to be expected from a global model.

As was the case for scattering by a slab (Section 3.1), the largest degree of polarization is obtained when the last scattering is through an angle close to a right angle. However, photons with $\theta\sim\pi/2$ cannot escape and peak polarization ratio is found for $\theta\sim45°$ and $\sim135°$. When $\tau_0\lesssim2$, the maximum polarization ratio is $R_{\rm P}\sim0.01$; roughly half the photons are scattered once and most of the remainder traverse the Sobolev surface unscattered. The polarization is almost symmetrical with respect to $\theta=\pi/2$, reflecting the symmetry of the cross-section and the preponderance of single scatterings. When $\tau_0\gtrsim2$, the polarization ratio diminishes and back-scattering starts to dominate. This asymmetry has its origin in the location of the photon source. The first scattering usually occurs before the resonant surface is reached and, on average, the photon has a negative Doppler shift. It is therefore less likely to diffuse in velocity-space and escape with a positive Doppler shift than to be reflected spatially and escape with $\Delta<0$. It is found that when $\tau_0\sim10$, 56 per cent of the photons are reflected at a Sobolev surface.

4.4.2 *Isotropic expansion*

As a second example of local scattering at a Sobolev surface, we consider a locally isotropic expansion – a 'Hubble' flow. This is appropriate for purely radial expansion with $V_r\propto r$. In Fig. 4(a) the degree of polarization and the emergent photon flux are shown as a function of $\mu\equiv\cos\theta$ for different τ_0. The results are quite similar to those found for the parallel expansion except that highly polarized photons once-scattered through $\sim\pi/2$ can now escape. The peak polarization ratio for side-scattering is now ~0.02 for $\tau_0\sim2$. Again strong back-scattering is apparent at large optical depth.

4.4.3 *Perpendicular expansion*

For our third, simple example, we suppose that the flow expands almost entirely transversely $[\tau(\mu)=\tau_0/(1-\mu^2)]$. This is a model of a spherical outflow with nearly constant radial velocity. Here, the escape of low-polarization forward- and back-scattered photons is inhibited and effectively all normally incident photons are scattered once. $R_{\rm P}$ is increased further to a peak value $R_{\rm P}\sim0.04$. In this case the bias to back-scattering sets in at a lower value of the transverse optical $\tau\gtrsim1$ (cf. Fig. 4b).

4.4.4 *Converging flow*

In order to illustrate the changes introduced when there is a simple, converging flow such as might be associated with a shock front, we suppose that the velocity gradient is negative along the propagation direction of the incident photon and positive along the two orthogonal directions. It is assumed that the absolute values for the velocity gradients are equal, i.e. $\tau(\cos\theta)=\tau_0/(|1-2\cos^2\theta|)$. Since the Sobolev optical depth goes to infinity at $\mu\equiv\cos\theta=\pm2^{-1/2}$, there are local minima in those directions in the polarized flux. A

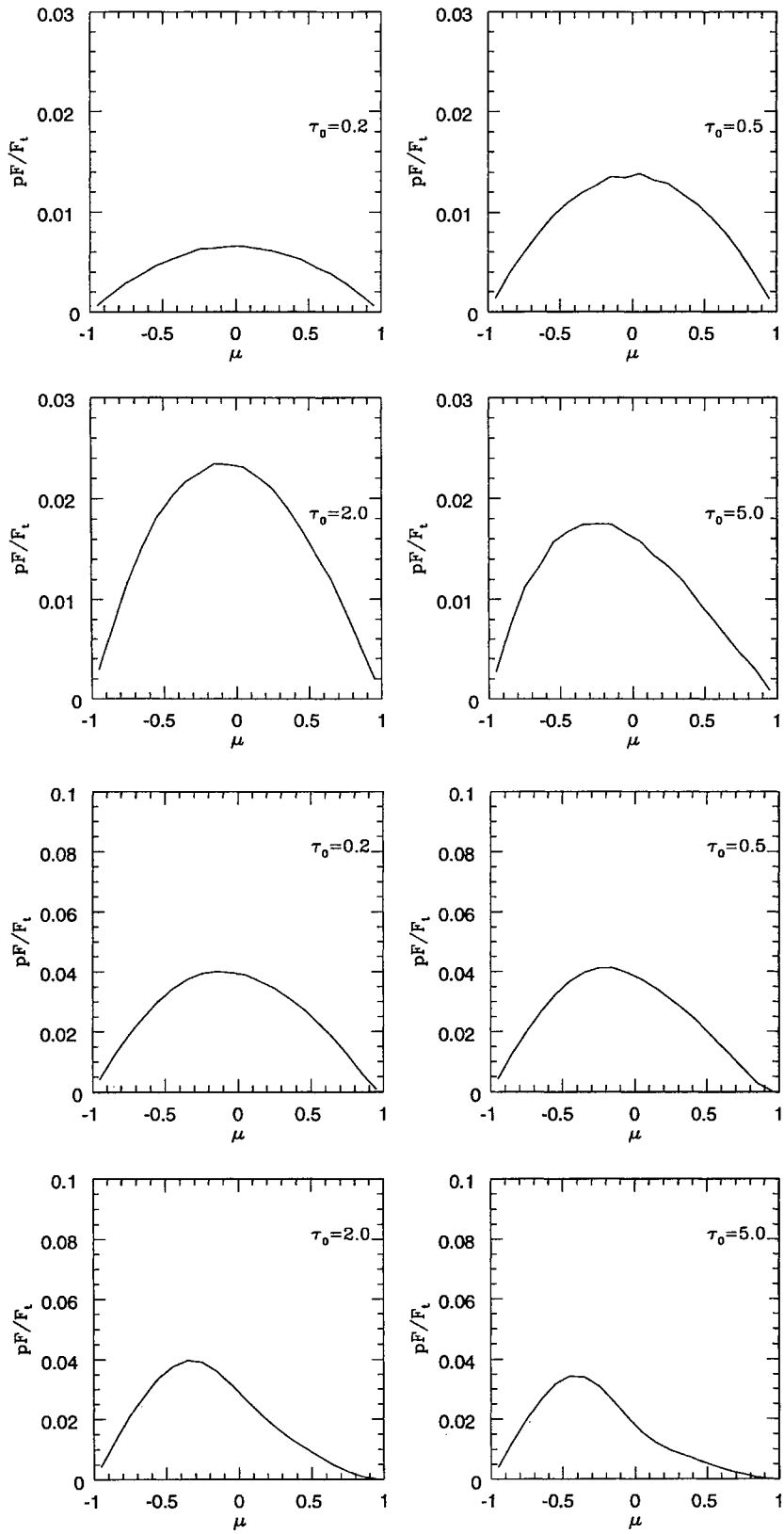

Figure 4. (a) Polarized flux per srad of scattered photon from a singlet Sobolev surface ($J=0\rightarrow1$) for a flow expanding isotropically with respect to the incident continuum source. The velocity field is given by $\boldsymbol{V}=\boldsymbol{V}_0+\boldsymbol{V}'(x\hat{x}+y\hat{y}+z\hat{z})$, where $\boldsymbol{V}_0$ and $\boldsymbol{V}'$ are constant. The Sobolev optical depth is given by $\tau_{esc}(\mu)=\tau_0$, where $\mu=\cos\theta$ is the cosine of the angle between the wavevector of the scattered photon and the line of sight. The normalization is given by the total incident flux. (b) Same quantity as in (a) for perpendicular expansion. The velocity field is given by $\boldsymbol{V}=\boldsymbol{V}_0+\boldsymbol{V}'(x\hat{x}+y\hat{y})$, where $\boldsymbol{V}_0$ and $\boldsymbol{V}'$ are constant. The Sobolev optical depth is given by $\tau_{esc}(\mu)=\tau_0/(1-\mu^2)$.

peak value $R_P \sim 0.03$ is achieved at $\tau_0 \sim 2$ and the forward–backward asymmetry begins to show up at $\tau_0 \sim 5$.

4.5 Scattering at a doublet Sobolev surface: $J = 1/2 \rightarrow 1/2$, 3/2

Resonance scattering by ions that are isoelectronic with Li atoms such as C IV, N V and O VI is more complicated when the velocity in the flow changes by more than the doublet (D) separation, expressed as a velocity. (We are indebted to Ray Weymann who urged us to consider the feasibility of separating doublets in polarization.) This appears to be relevant for BALR in contrast to individual BEL clouds, because the absorption-line profiles are known to be smooth, implying that there are no gaps in velocity-space along a typical line of sight at a resolution ~ 8 km s^{-1} (Barlow & Junkkarinen, in preparation).

Consider first a single photon emitted by the central continuum source and incident upon an expanding outflow. Let its wavelength be blueshifted with respect to the emission line by a velocity $\sim 20\,000$ km s^{-1} say, so that it lies outside the emission line and well within the observed trough. The first resonant velocity surface that it will encounter is that associated with the $J = 1/2 \rightarrow 3/2$ transition. Dependent upon the Sobolev optical depth along its direction of propagation it may be scattered one or more times within a distance corresponding to a few thermal widths of its original resonant surface. It will emerge along a new direction with a frequency that is almost identical to its initial frequency when measured in the fluid rest frame, but which will be redshifted by typically $\sim 20\,000$ km s^{-1} in the AGN frame. On average it will be polarized. If the fluid is expanding in all directions about the original point of resonance, then the photon will have a second opportunity to scatter as it encounters the $J = 1/2 \rightarrow 3/2$ resonance. The optical depth will be reduced from that for the $J = 1/2 \rightarrow 3/2$ by one factor of 2, to account for the different statistical weight of the transition, and changed by the inverse ratio of the velocity gradient along the propagation direction. If there are one or more scatterings at this second resonance, then this time the emergent photon will, on average, be unpolarized. It will also be emitted isotropically. *One scattering in the* $J = 1/2 \rightarrow 1/2$ *resonance suffices to erase all memory of the incident direction of propagation and polarization.* At large optical depth, resonantly scattered photons will be isotropized and depolarized. At small optical depth, a few photons will be scattered once in the $J = 1/2 \rightarrow 3/2$ resonance and most of these will escape with no further $J = 1/2 \rightarrow 1/2$ scattering and emerge with high polarization.

4.5.1 *Parallel expansion*

We carry out a Monte Carlo simulation to the parallel expansion case discussed for the $J = 0 \rightarrow 1$ case. The only changes that are necessary are to modify the radiation pattern and the polarization of the radiation scattered at the $J = 1/2 \rightarrow 1/2$ resonance. If they are scattered, then they emerge isotropically without polarization. As before, at small optical depth, the scattering is mainly in the forward and backward directions. Therefore those photons that do avoid $J = 1/2 \rightarrow 1/2$ scattering have a low polarization on average. Thus the emergent polarization is very small ($R_P \sim 0.001$) and for $\tau \gtrsim 2$, the polarization effectively vanishes.

4.5.2 *Isotropic expansion*

As might be expected from the foregoing discussion, a larger degree of polarization ensues when side-scattering is allowed ($R_P \lesssim 0.006$). The rapid decrease in R_P for $\tau_0 \gtrsim 2$ is deduced from the fact that the unpolarizing $1/2 \rightarrow 1/2$ resonance photons contribute increasingly to the scattered radiation field. The forward–backward asymmetry shows up $\tau \sim 5$. However, due to the rapid decrease of R_P the polarization is negligible for $\tau \gtrsim 10$ (cf. Fig. 5a).

4.5.3 *Transverse expansion*

When sideways scattering is required, we find a peak value $R_P \sim 0.02$, i.e. about half the value for the $J = 0 \rightarrow 1$ resonance (cf. Fig. 5b). However, the polarization rapidly decreases with increasing τ for the same reason as in the preceding case.

4.5.4 *Converging flow*

A maximum value of $R_P \sim 0.01$ is seen when $\tau_0 \sim 1$, which is comparable to the perpendicular expansion case. The polarization behaviour is also similar to the perpendicular expansion except for the existence of local minima in R_P because of the infinite optical depth at $\mu = \pm 2^{-1/2}$. Since the flow is contracting in the directions with $|\mu| \leq 2^{-1/2}$, all the photons scattered in those directions are out of resonance with the transition $J = 1/2 \rightarrow 1/2$. These photons escape without further scattering and hence do not suffer any depolarization. For $\tau_0 \gtrsim 5$ the local minima in R_P disappear and the only observable polarized flux is seen in the directions with $|\mu| \leq 2^{-1/2}$.

4.6 Scattering at multiplet Sobolev surfaces – Lyα–N V

Lyα emission lines are rarely prominent in BALQs. This is usually attributed to absorption of the emission line by outflowing N V ions. The N V doublet (separation 970 km s^{-1}) is separated from the Lyα blended doublet (separation 1 km s^{-1}) by a velocity $\Delta V = 5900$ km s^{-1}. This is a significant fraction of the width of the whole absorption trough. On the presumption that the initial spectrum at the base of the acceleration contains a flat continuum plus a broad, blended Lyα–N V emission line, Turnshek (1988) and Arav, Li & Begelman (1994) have proposed that the outflowing BAL gas should be subject to mild line-locking. Specifically, they suggest that the radiative acceleration of the gas increases and then decreases as the N V ions move into and then out of resonance with the blended emission line. The velocity history is then imprinted in the trough of a more passive ion, like C IV, which should show less absorption at a blueshift of ~ 5900 km s^{-1}, relative to the Lyα–N V emission line. Korista et al. (1993) report possible observation of this effect in the spectra of a minority of BALQs.

In attempting to assess the prospects for polarimetry, we should note that the Lyα doublet, which will be encountered first by photons of a given frequency in the AGN frame, has a separation (~ 1 km s^{-1}) much less than the local thermal

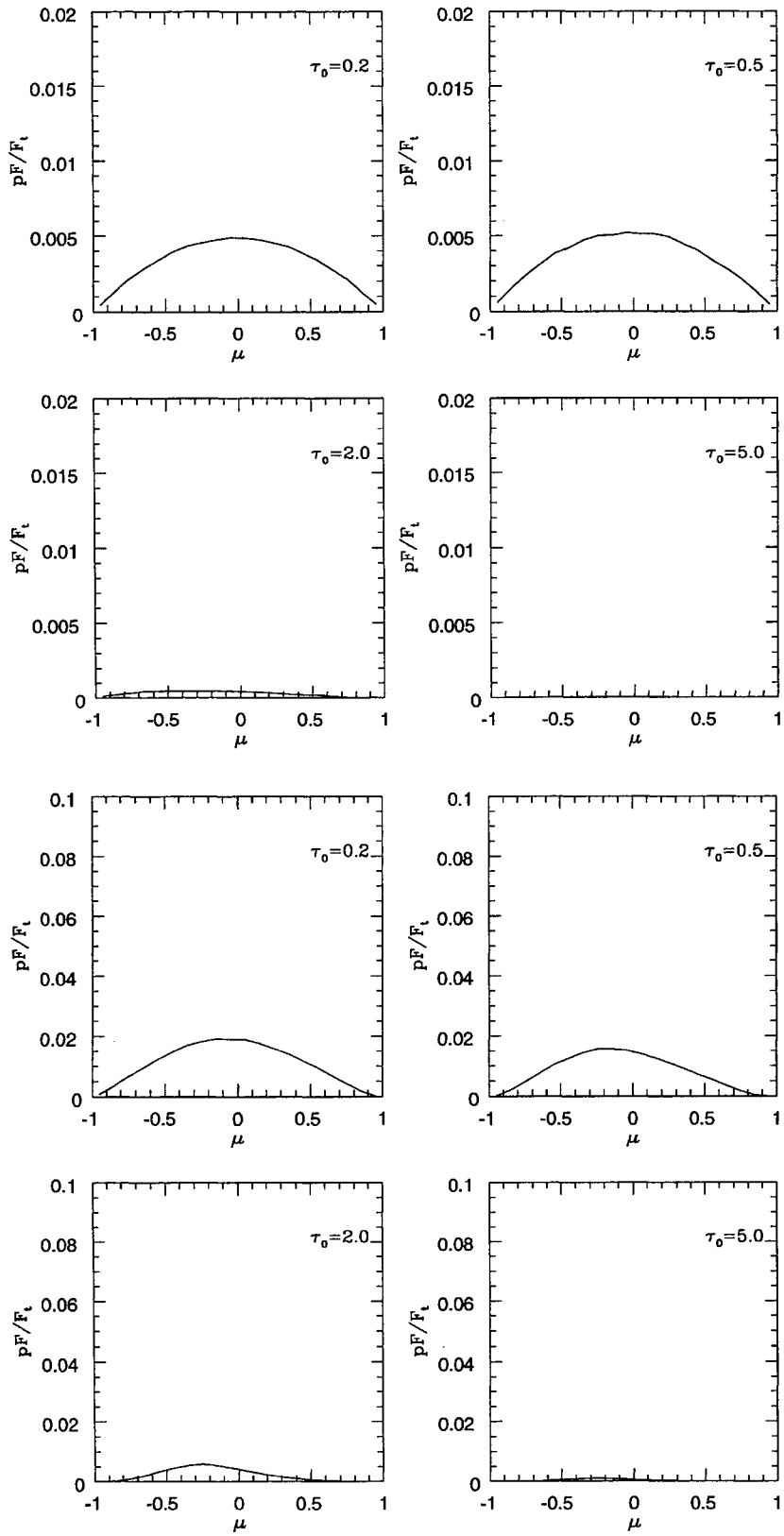

Figure 5. (a) and (b): same quantities as Fig. 4(a) for the $J = 1/2 \rightarrow 1/2, 3/2$ doublet.

width. Using the formalism of Paper I we can then compute the polarization to be expected after a single scattering through an angle θ. We find that

$$P(\theta)=\frac{3\sin^2\theta}{11+3\cos^2\theta}, \tag{4.13}$$

which will be intermediate between the value $P(\theta)=3\sin^2\theta/(7+3\cos^2\theta)$ for $J=1/2\rightarrow3/2$, and the value $P(\theta)=0$ for $J=1/2\rightarrow1/2$. As the optical depth in the Lyα transition is likely to be substantial, we expect that these photons will emerge from their local Sobolev scatterings significantly depolarized. At wavelengths sufficiently close to 1240 Å, where the N v resonance can also be encountered, the polarization behaviour will be similar to that described in Section 4.5. As the scattering associated with the Lyα–N v resonances is quite non-local, the expected polarization is quite model dependent.

4.7 Radiative mixing of higher multiplet transitions

Although many of the most prominent resonance lines are simple singlets and doublets like those already considered, there are several more complex multiplet transitions and these may also contribute to the net polarization. These lines allow several choices for the total angular momenta of the ground and excited states and the permitted transitions have to be considered collectively. The polarization can be computed according to the principles we have already described, although there are three complicating factors. First, some multiplet lines have frequency shifts lower than the Doppler shifts associated with the ion thermal motion. This means that the ground energy levels are effectively degenerate so that scattering in the different components occurs effectively simultaneously (as with Lyα), not successively (as with C IV). Secondly, when the ground state angular momentum satisfies $J_g\geq1$, radiative mixing of the ground sublevels leads to significantly enhanced polarization (cf. Paper I, section 4.2) relative to that computed for collisional mixing. Thirdly, in order to compute the radiative mixing correctly, all ground state transitions, not just those in a given multiplet, must be included to derive the distribution of ions among ground state sublevels.

For the common, low-Z, ions, there are three further cases to consider, beyond Li- and Be-like ions. First, we consider ions that are isoelectronic with B atoms, such as C^+, N^{++} and O^{3+}. Here, the ground levels are $^2P^0_{1/2,3/2}$, with the $J_g=1/2$ state having the lower energy and the splitting exceeding the Doppler width. The excited states to which excitations are permitted are $^2S_{1/2}$, which gives unpolarized doublets (D′), $^2D_{3/2,5/2}$, giving rise to triplets (T) and $^2P_{1/2,3/2}$ which produces quadruplets (Q). All lines are distinct. An important example is the O IV ion, where the lines with significant oscillator strength are λ789(T), 609(D′), 554(Q), 238(T). (Only the λ789 triplet has been observed in BALQ spectra: Korista et al. 1993; Arav, private communication.) The relative frequency of these different excitations depends upon the spectral index, with the longer wavelength transitions being more prominent for steeper spectra.

In Appendix A, we summarize how to compute the polarization under conditions in which a multiplet is present and the radiation field is axisymmetric with respect to the outward radial direction. The scattered radiation also exhibits this symmetry and the scattered radiation will only be polarized parallel and perpendicular to the $\boldsymbol{k}$–$\hat{\boldsymbol{r}}$ plane. The results are expressed as a scattering matrix that relates the polarization state of the scattered radiation to the polarization of the incident photons. We have computed the polarization in the various O IV multiplet transitions assuming an isotropic expansion of variable optical depth. We find that as a consequence of the interplay between the different transitions, the population of the ground state sublevels is closer to statistical than in the simple (and fictitious) two-level ions considered in Paper I. This reduces the net observed polarization.

The incident radiation field is assumed to be given by a power law

$$F_\nu\propto\nu^{-\alpha}. \tag{4.14}$$

We consider two cases, $\alpha=1$ and 3. Most of the multiplet transitions are not highly polarized. In the case of doublet D′ no polarization is obtained, because the excited-state sublevels are always populated evenly so that an isotropic re-emitted radiation field results. The highest polarization is shown in the triplet transition (T) where $p\lesssim0.01$. Fig. 6 shows the result for a range of optical depths.

The second case that we must consider involves ions that are isoelectronic with C atoms, such as N^+ and O^{++}. Here the ground state is $^3P_{0,1,2}$. One possible excited state is $^3S^0_1$, which produces unpolarized triplets (T′). Another possible excited state is $^3P^0_{0,1,2}$, which gives six transitions (S) satisfying the selection rules. However, it turns out that the $J_e=1$, 2 energy levels are effectively degenerate and only four distinct lines are formed. The final case is $^3D^0_{1,2,3}$, where again there are six possible transitions (S′) and the degeneracy of the $J_e=1$, 2 states reduces the number of lines to four. The most important O III lines are λ835(S′), 703(S), 508(T′) and 305(S′), of which the first two lines have been reported. Lines associated with the S′ multiplet should be comparably polarized to T multiplet lines.

The third common case involves ions that are isoelectronic with N atoms, such as O^+. The ground state is $^4S^0_{3/2}$ and the excited state is $^4P_{1/2,3/2,5/2}$. This produces a different type of triplet line that is relatively strongly polarized. Prominent examples include O II λ835, 539 and S II λ1256.

There is one additional possible complication that we have chosen not to consider, and this is that there may be significant scattering from ions in metastable excited states. In particular, if the UV spectrum is sufficiently hard, the rate of photoionization from the ground state can be as large as ~0.2 of the excitation rate. The subsequent recombination may leave the ion in a state with a different value of S (six possible transitions). In the case of O^{3+}, there are no permitted transitions from states with $S=3/2$ to states with $S=1/2$ and so recombination into a state with $S=3/2$ will be followed by a cascade down to a metastable state. In a sufficiently tenuous gas where collisional de-excitation can be ignored (as will generally be the case for BALQ flows), the fraction of ions in the metastable state will be given roughly by the ratio of the photoionization rate to the A-value for the intercombination line. In the case of O^{3+}, $A_{\rm intercomb}$ is $\sim2\times10^3$ s^{-1}. We estimate the ratio of the strength of the intercombination line to the permitted lines

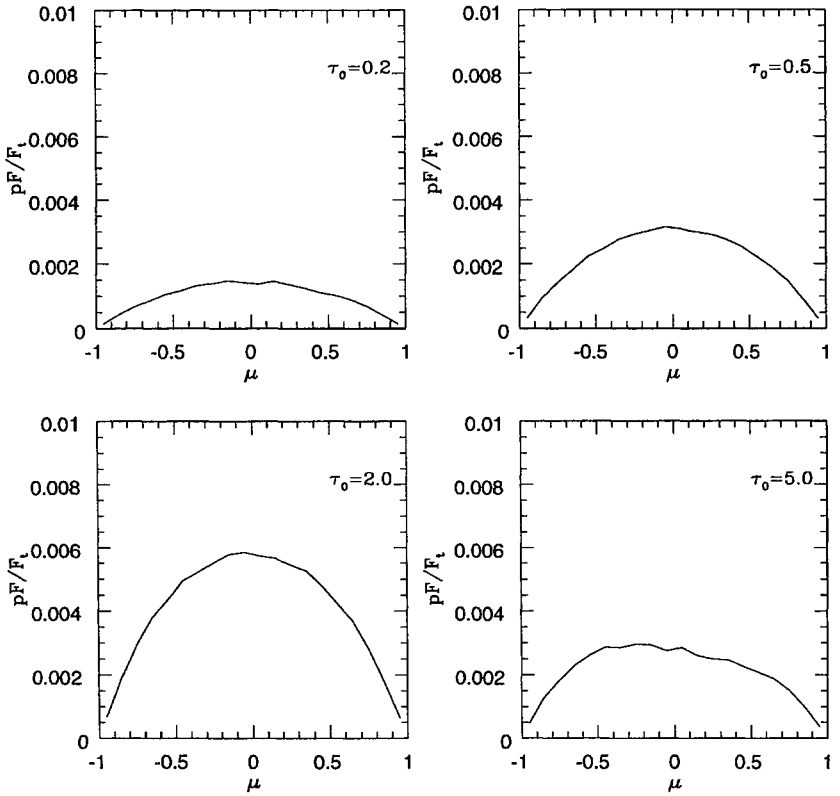

Figure 6. Same quantities as Fig. 4(a) for the triplet $^2P_{1/2,3/2} \rightarrow {}^2D_{3/2,5/2}$, where the incident spectrum is given by a power law where $\alpha = 1$.

to be ~ 0.1 ($\alpha = 1$), ~ 0.01 ($\alpha = 3$), and so it should not seriously alter the ground state sublevel populations. (A quantitative measure of the importance of intercombination transitions is provided by observation of permitted transitions from the metastable state. Interestingly, tentative evidence for such a transition in O^{4+} has been presented by Korista et al. 1993).

5 GLOBAL OUTFLOW MODELS

We next turn to considering global models in which there is a large-scale flow so that photons that emerge along a particular direction can have their last scattering anywhere along a particular extended Sobolev surface parametrized by their Doppler shift. We assume that photons originate within a compact central continuum source located at the origin and propagate outward until they encounter a Doppler surface where the frequency in the rest frame of the gas equals the natural frequency of the resonance transition. At this point they are scattered into a direction and with a polarization determined probabilistically by the local Sobolev optical depth and the velocity gradient tensor. The scattered photons are then allowed to scatter again if they encounter additional resonant surfaces as they emerge from the nucleus. In this manner, the photons incident upon the Sobolev surface corresponding to the final scattering can arrive from a variety of directions and so the observed polarization can be diminished.

Our approach is similar in many respects to that of Hamann et al. (1993). However, there are three important innovations. First, by using a Monte Carlo approach, we can track the polarization. Secondly, we consider non-radial flow fields which allow non-monotonic velocity variation along a line of sight despite steady expansion along a given streamline. Thirdly, we also allow for the presence of angular momentum, which as we shall see introduces some important kinematic changes (cf. Murray et al. 1995).

5.1 Disc and conical wind

As a first example and as a check on our code, we consider the kinematic model proposed by Hamann et al. (1993) who calculated the line profiles formed in conical or disc-like winds with radial velocity law $V_r \propto r^\gamma$, where $\gamma = 1$. This is similar to the isotropic expansion prescription considered above. The optical depth prescription, which Hamann et al. introduced and we adopt, is given by a function of radial velocity which has the maximum value 2 for velocities 4000–6000 km s^{-1} and the covering factor is $q = 0.25$. Hamann et al. used the escape probability formalism to construct line profiles. As a check on our formalism, we reproduce their total intensity distributions using our Sobolev–Monte Carlo approach and, in addition, compute the degree of polarization for the transition $J = 0 \rightarrow 1$ (Fig. 7a).

The incident continuum is assumed to be unpolarized and hence the polarization is solely due to the scattered component, which is shown by the dotted lines. The scattered component is approximately symmetric with respect to the line centre and the polarized flux shows similar symmetry. This approximate symmetry is explained by the low optical depth $\tau \lesssim 2$ adopted in this problem, where single-scattering dominates. However, the degree of polarization is fairly

large (~ 0.1) in the absorption trough since the ratio of the scattered component to the transmitted continuum component is significantly higher than that in the emission part. The polarization direction is parallel to the projected disc axis, confirming that the polarized flux is dominated by side-scattering.

In Fig. 7(b) the disc wind with angular momentum is considered. The velocity field is given by $V \propto [r\hat{r} + A\hat{\phi}/(r \sin\theta)]$, where A is constant. A is chosen to satisfy $V_\phi/V_r = 0.2$ at the point where $V_r = 18\,000$ km s^{-1}, $\theta = \pi/2$. The addition of an azimuthal velocity component introduces an additional Doppler shift to the scattered photons, so that a different absorption trough is obtained. The dramatic reduction of the degree of polarization implies that the photons filling in the trough originate from the parts of the disc having angles larger than or smaller than 90° with the observer's line of sight.

A similar absorption profile is obtained from a conical wind model with the same covering factor as in the disc wind case. However, the degree of polarization in the absorption trough is small (~ 0.02) compared with the case of the disc wind. This is due to the dominance of forward-scattering.

When an azimuthal component is introduced into this conical wind there is little difference in polarization from the purely poloidal flow. This is explained by the fact that the azimuthal motion does not affect the forward scattering which is responsible for the dominant polarized flux in the conical wind.

5.2 Equatorial flow

For our second, global model we consider an equatorial flow where the BAL material accelerates on hyperboloid surfaces to an asymptotic speed that is inversely proportional to the square root of the radius of the foot point of the flow (cf. Appendix A). We consider both purely poloidal flow and flow with an azimuthal component. Fig. 8 shows a truncated section of a Sobolev surface for a flow with angular momentum for an observer lying on the x–z plane with colatitude $\theta_0 = \pi/3$. The viewpoint is the observer's line of

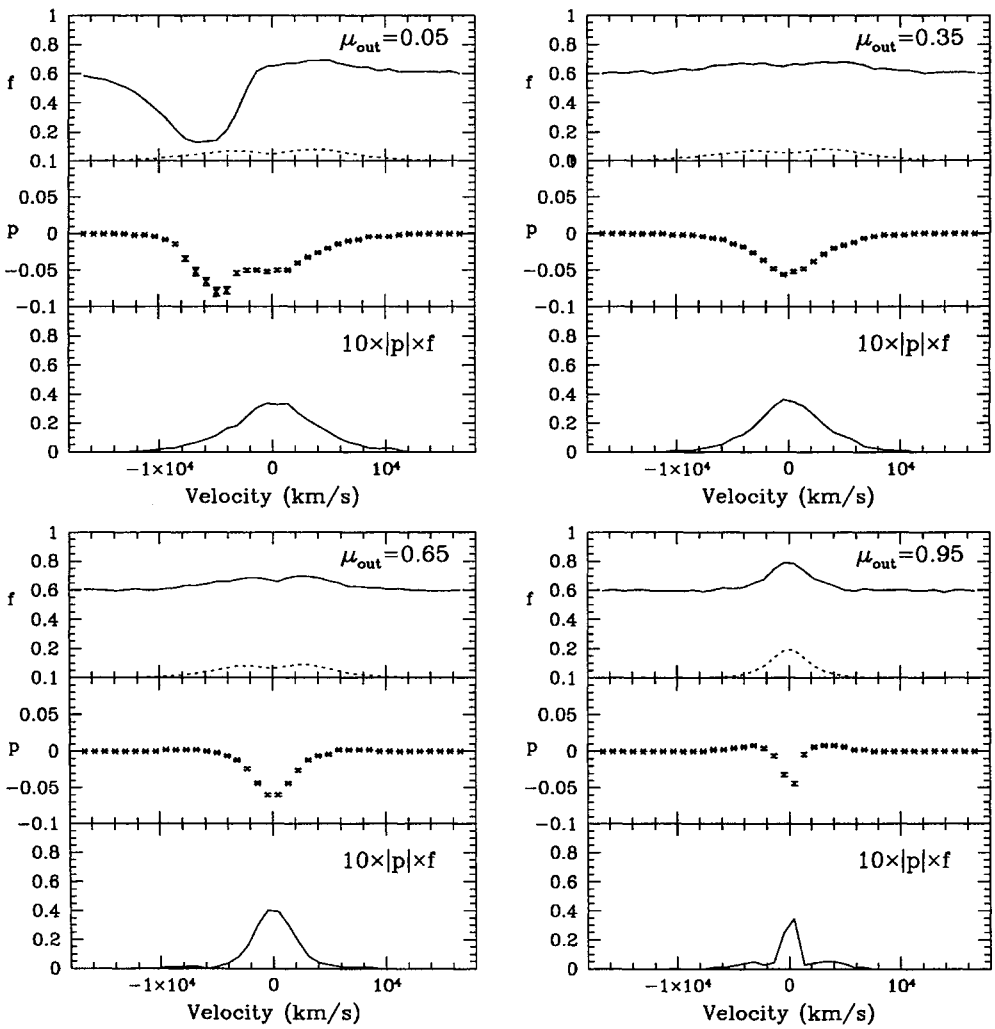

Figure 7. (a) Total flux, polarization and polarized flux from disc wind models by Hamann et al. (1993). The velocity is given by $V \propto r\hat{r}$ and the covering factor is $q_{\rm disc} = 0.25$. (b) The total flux, polarization and polarized flux from the same model as in (a), with additional azimuthal velocity component. The velocity is given by $V \propto [r\hat{r} + A\hat{\phi}/(r \sin\theta)]$, where A is constant. A is chosen to satisfy $V_\phi/V_r = 0.2$ at the point where $V_r = 18\,000$ km s^{-1}, $\theta = \pi/2$.

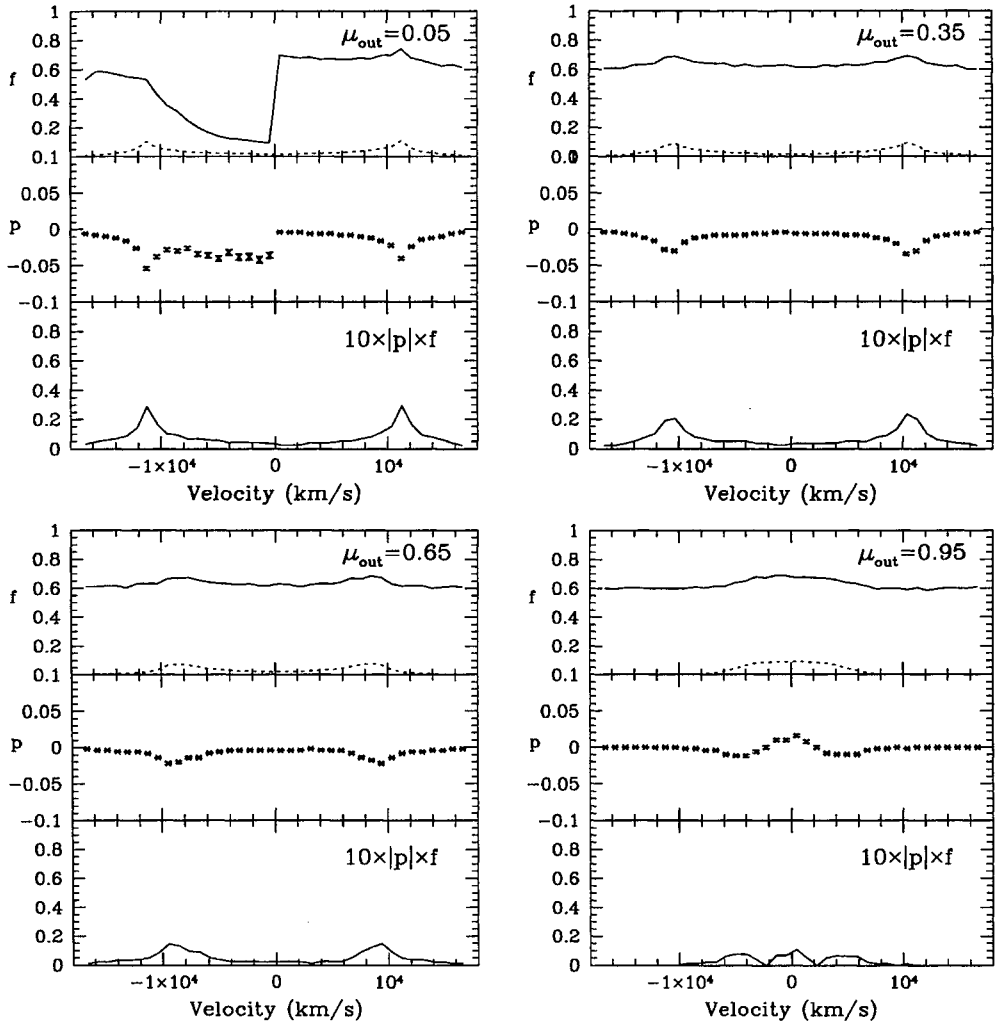

Figure 7 – *continued*

sight and the illuminated side is the part lying in the $-x$ direction from the central continuum source. Unlike Hamann et al.'s model, considered in the preceding section, scatterers are not confined to a region with a small covering factor but flow throughout a large volume in a manner that conserves mass. In our model, the optical depth increases toward the equatorial plane so that the Sobolev surface with moderate optical depth ($\tau_{\rm Sob} \gtrsim 1$) is only present at low latitude (see also Appendix A). It is more likely that the absorbing clouds expand as they flow radially outward, which would tend to decrease the Sobolev optical depth as a function of blueshift.

The radial velocity component along the line of sight has a minimum near the centre, which corresponds to the sharp cut-off at the broad absorption trough in the line profile. The Sobolev optical depth along the radial direction is much larger than 1 when $\mu = \cos\theta \to 0$ and much less than 1 as $\mu \to 1$.

Fig. 9(a) shows the polarization that results from a purely poloidal flow, simulated using 10^7 photons. The parameters are chosen so that the Sobolev optical depth $\tau_{\rm Sob} = 1$ at $-\Delta V = 1.7 \times 10^9$ cm s^{-1} in the direction $\mu = 0.2$. Here, the maximum degree of polarization in the absorption trough is ~ 0.5, which results from side-scattering at low latitude. The polarized flux ratio defined in the preceding section is $R_{\rm P} \sim 0.03$ in this case. Outside the trough, the radiation is unpolarized. The negative degree of polarization signifies that the electric vector is parallel to the symmetry axis. The maximum degree of polarization coincides with the deepest absorption of the line, because the unpolarized transmitted component contributes least here. However, the polarized flux extends to the red side with peak value located in the blue side near the line centre. A closer look at the polarized flux also reveals a slight asymmetry with respect to the peak, which is reminiscent of the asymmetry encountered in the local analysis. It should be noted that the positions of peak values do not necessarily coincide with the position of the deepest absorption trough.

We next add azimuthal motion. The same parameters were chosen as in the case of purely poloidal flow and the constant specifying the azimuthal component (B in equation A3) is chosen to be 5. This shifts the negative polarization into higher Δv, where positive polarization dominates. The addition of azimuthal motion generally reduces the degree of polarization and the polarized flux. When the azimuthal component of the flow dominates the radial component,

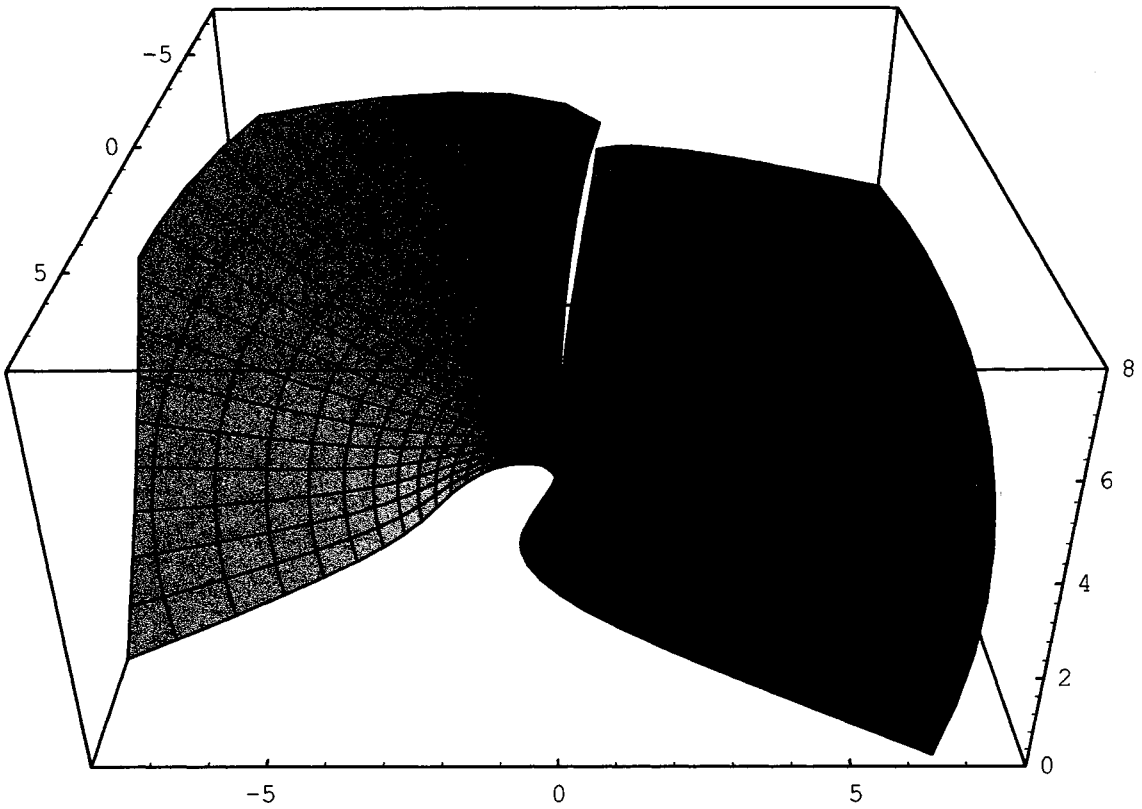

Figure 8. A typical Sobolev surface of an equatorial flow with angular momentum for an observer lying on the x–z plane with colatitude $\theta=\pi/3$. Each flow line lies on a hyperboloid ($\lambda=$constant in the oblate spheroidal coordinate system: see Appendix A), and the fluid element accelerates to an asymptotic speed (see text).

then the side-scattering gains large Sobolev optical depth towards the observer's line of sight, whereas the forward-scattering is relatively less affected by the azimuthal component. This leads to a change in the polarization direction. However, it should be emphasized that the polarized flux is much smaller than that in the case of purely poloidal flow. The absorption trough becomes deeper because a reduced number of photons scattered sideways fills in the trough, which also explains the decreased polarized flux.

We next consider the transition $J=1/2\rightarrow1/2$, 3/2 doublet case for a purely poloidal flow and a flow with angular momentum, where the multiplet separation is assumed to be much larger than the local thermal velocity. The largest degree of polarization from the purely poloidal flow is ~0.15 at the absorption trough, and the polarized flux ratio is $R_{\rm p}\sim0.008$. Apparently the contribution of unpolarized $J=1/2\rightarrow1/2$ photons is not large in this case. Again as shown in Fig. 9(b) the addition of angular momentum leads to reduced polarized flux and in the case of high angular momentum, the polarization direction changes. The peak value for the degree of polarization in this case is ~0.1, but the polarized flux is no larger than 0.1 per cent that of the unpolarized continuum flux.

5.3 Bipolar flow

Finally, we consider another simple poloidal flow where the BAL material moves on a family of paraboloidal level surfaces. The Sobolev optical depth is calculated in a similar way to that described in the previous section. In this flow, however, the density function is chosen to be $n(\xi_2)$ (see Appendix C), which gives large optical depth to the jet direction. Here, the adopted velocity law gives a monotonically increasing velocity along the flow line but decreasing velocity along the radial line of sight from the central source to the observer. Hence, in contrast to the equatorial flow considered in the previous section, photons making the transition $J=1/2\rightarrow1/2$ hit the Sobolev surface first and then possibly they can be scattered at the second Sobolev surface associated with the transition $J=1/2\rightarrow3/2$.

The numerical results are shown in Fig. 10. In this bipolar flow case, the direction of polarization is perpendicular to the projection of the disc symmetry axis. The degree of polarization of the purely poloidal flow is ~0.15 and 0.05 for the $J=0\rightarrow1$ transition and the $J=1/2\rightarrow1/2$, 3/2 doublet respectively. The polarized flux ratios of $R_{\rm p}\sim0.02$ and 0.005 are obtained from the two cases respectively. The low degree of polarization and the polarized flux compared with the counterparts of an equatorial flow may be attributed to the dominance of forward-scattering over side-scattering. Different polarization behaviour between the $J=0\rightarrow1$ singlet transition and the $J=1/2\rightarrow1/2$, 3/2 doublet transition is attributed to the different Sobolev structures. Again, we consider the effects of azimuthal motion. Contrary to the equatorial flow, the degree of polarization changes little when angular momentum is introduced into the flow. This is

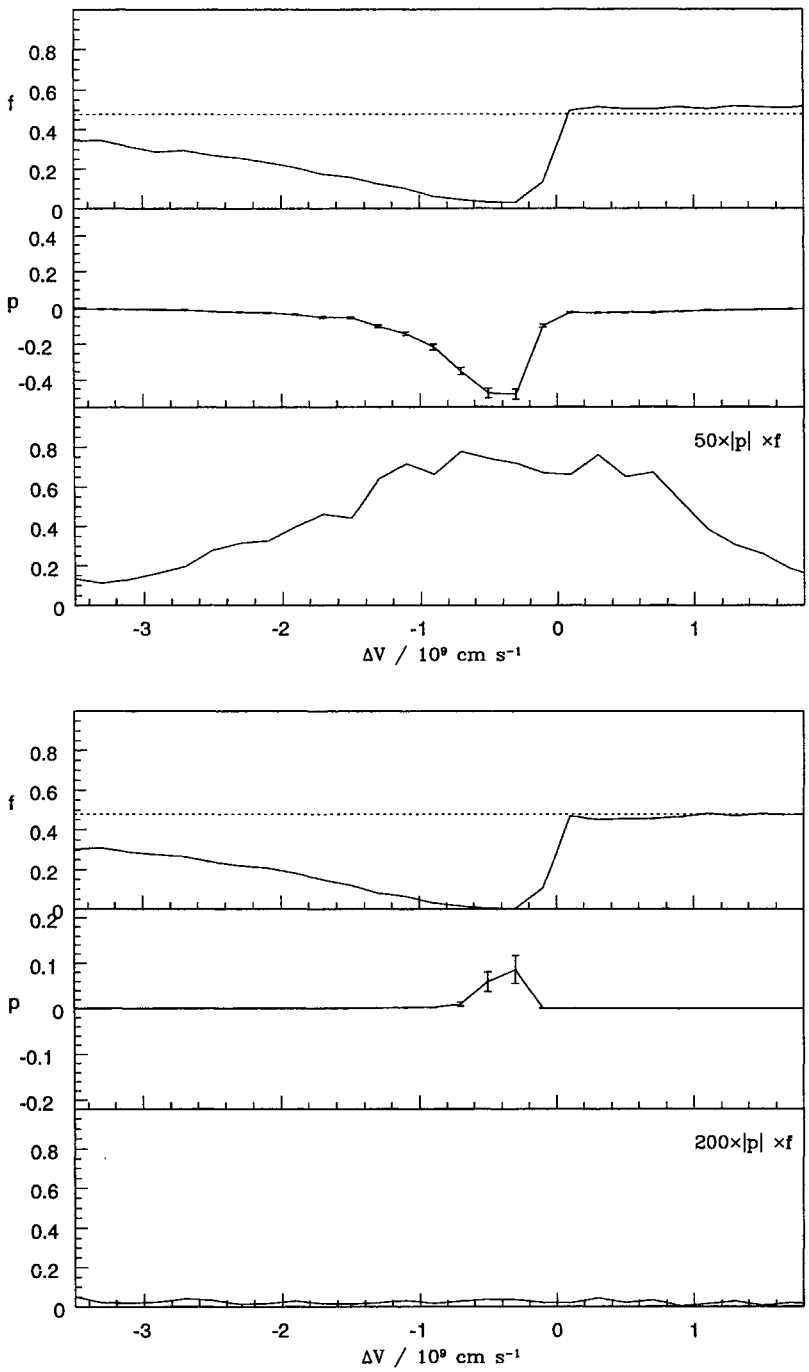

Figure 9. (a) Total flux, polarization and polarized flux pf from a purely poloidal equatorial flow for $J=0\rightarrow1$. The observer's line of sight is $\cos\theta=0.2$ and the parameters are chosen so that $\tau_{\rm Sob}=1$ at $\Delta V=-1.7\times10^9$ cm s^{-1}. See Appendix B for detail. (b) Total flux, polarization and polarized flux from an equatorial flow with angular momentum for $J=1/2\rightarrow1/2$, 3/2 doublet.

explained by the fact that the azimuthal motion does not affect the forward-scattering, which is also shown in the conical model discussed in the previous section. Since back-scattering is not important for the bipolar flow, the polarized flux is concentrated on the blue side, where absorption occurs. However, if the observer lies at low latitude, then the back-scattering may not be negligible. In this way bipolar flow can be distinguished from equatorial flow.

6 OBSERVATIONAL RAMIFICATIONS

In Section 2, we introduced a generic model for line formation by radio-quiet quasars involving a compact continuum source, a BELR and a scattering outflow. In Sections 3 and 4 we have discussed how spectropolarimetry can elucidate the geometrical and kinematical organization of these three components. We will now summarize what we have learned

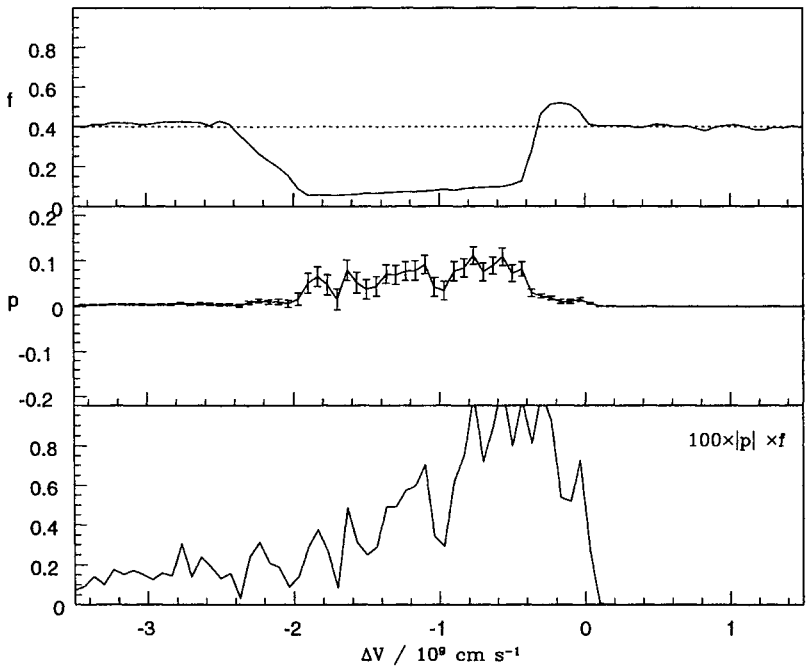

Figure 10. Total flux, polarization and polarized flux pf from a purely poloidal bipolar flow for $J=0\rightarrow1$. The observer's line of sight is $\cos\theta=0.8$ and the parameters are chosen so that $\tau_{\rm Sob}=1$ at $\Delta V=-1.7\times10^{9}$ cm s^{-1}. See Appendix C for detail.

from recent observations and outline some immediate possibilities for furthering our understanding of quasar line formation.

6.1 Interpretation of recent spectropolarimetric observations

The spectropolarimetric data base for radio-quiet quasars is sparse. The brightest example of a BALQ, PHL 5200, was first observed in this manner by Stockman, Angel & Hier (1981). More recently, Glenn, Schmidt & Holtz (1994) have presented observations of CSO 755 and Cohen et al. (1995) report upon Keck/Palomar data from PHL 5200 and 0105 – 266.

It appears that BALQs exhibit a modest ($p_{\rm C}\lesssim3$ per cent) continuum polarization that varies at most slowly in wavelength and constant position angle. Prominent UV emission lines, by contrast, appear to be unpolarized at about the ~0.5 per cent level. A possible exception is C III] $\lambda1909$, which Cohen et al. found to exhibit 1.3 per cent polarization in PHL 5200 in the same direction as the electron scattering (see also Goodrich & Miller 1995). If this pattern is verified by further observation, it will provide support for the standard model of emission-line regions in which the emitting gas moving at a given velocity occupies discrete contiguous regions (or clouds) in phase-space each with large resonance-line optical depths. Exterior to these clouds, however, the BELR is optically thin at a given velocity along most lines of sight. Based on our calculations in Section 3, we estimate that the mean optical depth at a given velocity in small clouds is $\lesssim0.1$, which translates into a column density limit $M_{\rm H}\lesssim10^{19}$ cm^{-2} for gas moving with a speed that is within 10 000 km s^{-1} of the line centre, constraining the model of Shields et al. (1995). By contrast, a weak polarization in the C III] line was predicted in Paper II on the grounds that the optical depth within a single emission-line cloud was uniquely low ($\tau\sim1$–10) and that therefore this line should be emitted with a measurable polarization.

In the BALQs PHL 5200 and 0105 – 266, it appears that the absorption-line troughs are less deep in polarized flux and the degree of polarization can reach $p_{\rm C}\sim12$ per cent at intermediate velocity within the absorption trough (cf. Cohen et al. 1995). More relevantly, the ratio of the polarized flux in the troughs to the background continuum flux is typically $F_{\rm P}/F_{\rm C}\sim0.01$–0.02. The direction of the trough polarization vector is also apparently along the same direction as that of the continuum polarization. Although there appears to be velocity structure in the line polarization, it is not possible to decide whether or not there is additional polarization associated with the red wings of the emission line.

Fortunately, there are good prospects for resolving some of these uncertainties. High-dispersion spectroscopy in the vicinity of selected prominent resonance lines, combined with an atlas of weak lines, should enable a careful continuum level to be constructed. Let us suppose that we can define a continuum from the measured flux for $|V|\gtrsim30\,000$ km s^{-1}. It should then be possible to define a line profile, perhaps including very broad wings, that may consist of scattered resonance-line radiation. If we further assume that there is only significant absorption in the blue wing, then it should be possible to subtract the line polarization so as to determine the polarized contribution to the line flux at wavelengths blueward of any absorption trough. Finally, if the absorption is strong, then the measured radiation in the trough is probably scattered and its polarized flux can be measured.

As we have already emphasized, scattering of line radiation can take two forms, electron scattering and resonance-line scattering, and they are probably both present. Cohen et al. (1995) interpret their observations in terms of a simple model in which a minority of continuum photons are Thomson-scattered along a higher altitude ray so that they are less attenuated by the outflowing BAL gas than the unscattered, direct radiation. This explanation accounts naturally for the constancy of the polarization direction. However, the free electrons probably have to be co-spatial with the emission-line clouds, so that the emission lines emerge unpolarized.

Alternatively, adopting the standard interpretation of BALQ (cf. also Hamann et al. 1993; Cohen et al. 1995), we can assume that a fraction $q_{\rm BALR}\sim 0.1$ of the continuum photons with frequency in the interval $\sim(1.03\text{–}1.1)\,\nu_0$ of a prominent resonance line of frequency ν_0 are scattered by outflowing gas. These photons escape along different directions, possibly encountering other resonant Sobolev surfaces along the way and being rescattered. A minimum equivalent width for the resonance-scattered radiation, $W_\lambda\sim\lambda_0 q_{\rm BALR}\,V_{\rm BALR}/c\sim 10$ Å averaged over direction, seems unavoidable. Taking into account all the uncertainties, this is not inconsistent with the fluxes typically measured in absorption troughs.

As discussed in Section 4, three features determine the contribution to the polarized flux in a given line from an element of suitably ionized outflowing gas. First, the component of velocity resolved along the line of sight dictates the Doppler shift. Hence, the prevalence of blueshifted absorption points to a general outflow. Secondly, the scattering angle dictates the degree of polarization; side-scattering is highly polarized; forward- and back-scattering exhibit low polarization. The diminishing degree of polarization observed at the blue end of the trough is then consistent with a flow that accelerates to move along the line of sight. Thirdly, the local velocity gradient tensor determines the optical depth and its variation with direction. If the optical depth $\tau\gtrsim 1$, photons escape most readily along directions where the velocity gradient is largest. For the doublet transitions, this allows photons to be scattered sideways with substantial polarization in a slowly accelerating but expanding flow, and to escape extreme depolarization in the $J=1/2\rightarrow 1/2$ resonance at modest optical depth. The similarity between the polarization direction in the continuum and that in the trough constrains the model. In a bipolar outflow model (e.g. Hes 1995), the continuum must be polarized perpendicular to the symmetry axis; in an equatorial outflow model, the polarization direction will be parallel.

To be quantitative, the simulations presented in Section 4 show that a typical equatorial outflow with no angular momentum gives a polarized flux ratio $R_{\rm P}\sim 0.03$ and 0.01 and degree of polarization in the absorption trough ~ 0.5 and 0.15 for a singlet $J=0\rightarrow 1$ and a doublet $J=1/2\rightarrow 1/2, 3/2$ transition, respectively. The polarized flux extends to the red side because of back-scattering. From a bipolar flow the polarized flux ratio is typically found to be ~ 0.02 and 0.005 for the singlet and the doublet transitions respectively. The degree of polarization can reach up to ~ 0.15 and 0.1 correspondingly. The polarized flux, however, is prominent only on the blue side of the line.

One issue, covered briefly in Section 4 of Paper I, is the influence of magnetic field on the polarization of the scattered radiation. This may be considerable. A magnetic field breaks the degeneracy between the different ground state sublevels. The energy splitting is very small in comparison with the local thermal velocity dispersion. However, the mixing that follows de-excitation into this state will lead to randomization of the off-diagonal elements in the ground state density matrix prior to the next radiative excitation. For this to be important, we require that the classical cyclotron frequency $\sim 3(B/1\ \mu{\rm G})$ Hz exceed the radiative excitation time-scale, $\sim 10Uf(n_{\rm e}/10^7\ {\rm cm}^{-3})$ Hz, which, in turn, must exceed the collision frequency (cf. equation 4.3). This is likely to be satisfied in the case of magnetically confined clouds. Under these circumstances, it is convenient to work in basis states referred to the magnetic field direction instead of to the incident beam. As an ion passes through several cycles of excitation and de-excitation, the ground state density matrix will quickly approach a limit that is, in general, quite different from the limit in the unmagnetized, radiative mixing case. The scattered radiation then exhibits quite different polarization properties that will reflect the direction of the magnetic field and the transition involved. A more detailed discussion of the magnetic mixing case will be discussed elsewhere (cf. also Goldreich & Kylafis 1981, 1982).

6.2 Kinematical inferences

Assuming that resonance scattering contributes to the flux in the absorption-line troughs, we can use polarization observations to decide whether this scattered flux is present in the emission line and its redward extension as might be expected if receding gas is directly observable. If so, this would support an equatorial outflow model. However, if there are bipolar jets launched from an optically-thick accretion disc then only the approaching component will be seen and excess polarized flux should only be measured in the blueward extension of the line.

The actual shape of the absorption trough, which varies from line to line and object to object, also contains kinematic information. Its smoothness implies that the absorbing gas either comprises a continuous wind flow, as in the model of Murray et al. (1995), or many clouds, as in the model of e.g. Arav & Begelman (1994). If we adopt a covering solid angle for the BAL gas $\Omega_{\rm BALR}\sim 1$ srad and a total BAL column density $\sim 3\times 10^{20}$ cm^{-2}, then the wind discharge in a typical quasar with $L_{46}\sim 1$ is bounded by $\dot{M}\gtrsim 0.03(R_{\rm BALR}/1\ {\rm pc})\ {\rm M}_\odot\ {\rm yr}^{-1}$. If the troughs are partially filled with scattered radiation then this will automatically lead to a smooth profile as long as the lines are totally absorbing. With a thermal velocity dispersion in the absorbing gas ~ 10 km s^{-1}, this requires at least 3000 individual clouds along a line of sight. If these clouds are freely expanding then, whatever their initial size, they will expand to become almost contiguous in phase-space (i.e. they will form a wind) as they double their radius. One difficulty with a wind model (addressed by Murray et al. 1995) is that the ionization parameter will be $U\sim 10^6 L_{46}R_{\rm pc}^{-1}$, orders of magnitude larger than the value generally supposed for the range of ionization states observed in absorption. If the clouds are confined so as to maintain $U\sim 0.1$, then their characteristic sizes will be extremely small, $\lesssim 10^8 R_{\rm pc}^2 L_{46}^{-1}$ cm.

6.3 Dynamical considerations

The very presence of absorption-line troughs informs us that momentum is removed from the radiation field by the accelerating gas (e.g. Weymann et al. 1982). If we ignore a slight correction for preferential back-scattering, then the radial acceleration of a fluid element is

$$g_{\rm rad}=\left[V\frac{{\rm d}V}{{\rm d}r}\right]_{\rm tot}\sum_{\ell}\frac{\nu_{\ell}F_{\nu_{\ell}}}{Jc^2}[1-{\rm e}^{-\tau(\nu_{\ell},V)}], \tag{6.1}$$

where $\nu_{\ell}F_{\nu_{\ell}}$ is the radiative flux per ln ν_{ℓ} for each contributing line and J is the mass flux (cf. Arav & Begelman 1994). Equation (6.1) has the implication that if there are no significant non-radiative forces and the flow is purely radial, then

$$\sum_{\ell}\nu_{\ell}L_{\nu_{\ell}\Omega}[1-{\rm e}^{-\tau_{\ell}(\nu_{\ell},V)}]=\dot{M}_{\Omega}c^2, \tag{6.2}$$

where the subscript Ω denotes a quantity per srad. This is just an expression of momentum conservation. It is not clear how much radiative acceleration is associated with the far-UV (Korista et al. 1993). However, on the basis of this simple estimate, we can bound the mass discharge in a purely radiatively driven flow

$$\dot{M}\lesssim 10^{-2}L_{46}\Omega_{\rm BALR}\ {\rm M}_{\odot}\ {\rm yr}^{-1}. \tag{6.3}$$

It is then required that $R\lesssim 10^{17}L_{46}\Omega^{-1}$ cm, in order to have enough column density to produce deep troughs. This is smaller than the estimated size of the BELR. Although none of these estimates can be regarded as secure at this stage, it is clearly worth considering alternative accelerating agents such as cosmic rays (Begelman, de Kool & Sikora 1991), dust acceleration (Scoville & Norman 1995), thermal pressure (Weymann et al. 1982) and the magnetic field (EBS).

6.4 Continuum polarization

A long-standing puzzle concerning continuum observations of quasars is the low value observed for the linear polarization in the optical and UV continuum. In most cases the polarization is found to be $\sim$1–3 per cent (Stockman et al. 1979). Furthermore, in the case of radio-loud objects, the polarization direction is often found to be aligned parallel to the radio source axis. This behaviour is in marked contrast to the expectations of optically thick, geometrically thin accretion disc models, which usually have an electron scattering atmosphere that ought to impose a polarization perpendicular to the symmetry axis with a degree that can be as large as 12 per cent, depending upon the observer's latitude and the relative importance of absorptive and scattering opacity (e.g. Laor, Netzer & Piran 1990).

One way of reconciling these observations with the theoretical expectation of a disc flow is to suppose that accretion discs contain strong magnetic fields that can Faraday depolarize the emergent radiation. In order for this to occur, there must be a few radians rotation of the plane of polarization in the final Thomson scattering optical depth. This will occur for wavelengths

$$\lambda\gtrsim 1000\left(\frac{B}{1000\ {\rm G}}\right)^{-1/2}\ {\rm \AA}. \tag{6.4}$$

Field strengths as large as $\sim$100–1000 G have been invoked to drive accretion flows close to the black hole. [Note that if the radiation is approximately thermal with an effective temperature $T(r)\sim hc/3\lambda$, then condition (6.4) can be rewritten as a condition that the ratio of the magnetic pressure to the photospheric radiation pressure exceed 0.01, independent of wavelength. Again, this does not seem too difficult to satisfy.] The small wavelength-independent continuum polarization that is observed might be imposed externally through electron scattering, or it might be a limiting polarization from the disc atmosphere.

In a remarkable recent observation, Koratkar et al. (1995) (cf. also Impey et al. 1995) have used the *Hubble Space Telescope* to measure polarization blueward of the Lyman continuum and find that it increases to a value $\sim$10–20 per cent. Curiously, this apparent edge in the polarized flux is not matched by an edge in the total flux. It seems simplest to attribute this radiation to an increasing fraction of non-thermal synchrotron emission from a corona to thermal radiation from the disc with decreasing radius and increasing frequency (cf. Rauch & Blandford 1991). In this case, the strong differential rotation is likely to produce a toroidal magnetic field and a polarization vector parallel to the symmetry axis.

6.5 Unification and grand unification

The (by now) standard and unifying explanation for the difference between type 1 and type 2 Seyfert galaxies is that although they are similar types of AGN, the former is viewed at high latitude and the latter at low latitude, so that the central continuum source and the BELR are obscured by an orbiting torus. The broad permitted lines from Seyfert 2 nuclei are then supposed to be formed through reflection by free electrons at high latitude. This model is consistent with the observation that the polarization direction in Seyfert 2 galaxies is typically perpendicular to the projected radio source axes in contrast to the situation in Seyfert 1 galaxies where the polarization direction is parallel.

Now, although a few Seyfert galaxies exhibit comparatively narrow, blueshifted absorption lines, there are no cases where lines as broad as 30 000 km s^{-1} are seen. It is therefore not certain how to relate BALQs to their lower power, Seyfert counterparts. If we adopt the equatorial outflow model and suppose that they are related to the Seyfert 2 galaxies, then the fact that the polarization direction is maintained through the trough suggests that, if there is resonance-line scattering, then the polarization direction is perpendicular to the projected source symmetry axis, opposite to the prediction of the models. Conversely, if we suppose that BALs are bipolar outflows driven by radiation pressure in very powerful ionization cones (e.g. Wilson 1995), and that we only see the approaching jet, then the polarization will be perpendicular to the source axis, consistent with the models.

Theories of grand unification strive to relate radio-loud to radio-quiet sources. One of the most striking properties of BALQs is that they appear to be completely absent among radio-loud objects. If the outflow turns out to be equatorial,

then we should probably interpret this absence by deducing that it originates at such a small radius that it precludes the existence of a polar jet. If the BAL outflow turns out to be polar, then this will probably indicate that the jet speed is too low for there to be highly efficient acceleration of relativistic electrons, as is the case in expanding supernova remnants. The formation of relativistic jets may require the presence of a rapidly spinning black hole and the absence of a central cluster of mass-losing stars (e.g. Perry & Williams 1993; Blandford 1994; Scoville & Norman 1995), both long-lived characteristics of a galactic nucleus. It is therefore to be expected that radio-loud quasars should not exhibit polarized resonance scattering in the way that their radio-quiet counterparts do.

6.6 Observational tests

We conclude by summarizing the principal observational tests that can be used to diagnose BALQs. First, one of our basic hypotheses – that the continuum is uniformly polarized – can be substantiated through measuring the polarization in several more objects and over a broader range of wavelengths. Secondly, high-dispersion spectroscopy can be used to measure line profiles in both radio-quiet quasars and BALQs. It will be of particular interest to determine if the line wings are intrinsically irregular or smooth. If they are irregular, then this will rule out the presence of a strong scattering component. If, however, they are smooth and symmetric, then this may point to an electron-scattering origin. By contrast, broad, smooth yet asymmetric wings are a signature of resonance-line scattering. The net equivalent width of the resonance-scattering component may be as much as 10 per cent of the full line equivalent width, and the velocity width as much as 30 000 km s^{-1}. A particularly intriguing example is provided by the Mg II BALQ Mrk 231 (Smith et al. 1995). Thirdly, if there is evidence for resonance-line scattering in both radio-quiet quasars and BALQ, then, in the former case, the polarization of the emission lines can be measured in more objects to verify that they are generally unpolarized (excepting semiforbidden lines) but possess broad wings of polarized flux. The effect should be much stronger in singlet $J=0\rightarrow1$ lines than in the more common doublet transitions. The singlet lines expected to be prominent in absorption include C III 977, N IV λ765, O V λ630, Mg I λ2853, Al II λ1671 and Si III λ1207 (cf. Verner, Barthel & Tytler 1994). Finally, and this is the key result of this paper, if a resonance-scattered component can be detected, through either its total or, more convincingly, its polarized flux, then it should be a good diagnostic of the overall disposition of gas in the nucleus of the quasar (cf. Hamann et al. 1993). If only blueshifted resonance-line radiation is seen in BALQs, then this will be consistent with a bipolar jet model (which we observe from close to the jet axis). Alternatively, if the resonance-scattered radiation extends into the red wing of the BALQ, then this will be compatible with the more widely supported equatorial outflow model. Similar fluxes of partially polarized scattered resonance-line radiation should be seen in non-BAL radio-quiet quasars where the line of sight does not intercept the scattering gas. A more detailed analysis of the polarized line profile might reveal rotation in the outflow. Most interesting of all, though, would be the failure to detect any evidence of resonance-scattered radiation, which may call into question the standard interpretation of quasar BALs.

ACKNOWLEDGMENTS

We are indebted to several colleagues, notably Ski Antonucci, Nahum Arav, Marshall Cohen, Bob Goodrich, Ari Laor, Norm Murray, Patrick Ogle and Ray Weymann for invaluable discussions and helpful suggestions. Support under NSF grant AST 92-23370 and NASA grant NAGW 2372 is gratefully acknowledged.

REFERENCES

Antonucci R. R. J., Miller J. S., 1985, ApJ, 297, 621
Arav N., Begelman M. C., 1994, ApJ, 434, 479
Arav N., Li Z. Y., Begelman M. C., 1994, ApJ, 432, 62
Begelman M. C., de Kool M., Sikora M., 1991, ApJ, 382, 416
Barlow T. A., Junkkarinen V. T., Burbidge E. M., Weymann R. J., Morris S. L., Korista K. T., 1992, ApJ, 397, 81
Blandford R. D., 1994, ApJS, 90, 515
Cohen M. H., Ogle P. M., Tran H. D., Vermeulen R. C., Miller J. S., Goodrich R. W., Martel A. R., 1995, ApJ, 448, L77
Corbin M. R., Francis P. J., 1994, AJ, 108, 2016
Emmering R. T., Blandford R. D., Shlosman I., 1992, ApJ, 385, 460 (EBS)
Glenn J., Schmidt G. D., Foltz C. B., 1994, ApJ, 434, L47
Goldreich P., Kylafis N. D., 1981, ApJ, 243, L75
Goldreich P., Kylafis N. D., 1982, ApJ, 253, 606
Goodrich R. W., Miller J. S., 1994, ApJ, 434, 82
Goodrich R. W., Miller J. S., 1995, ApJ, 448, L73
Hamann F., Korista K. T., Morris S. L., 1993, ApJ, 415, 541
Hes R., 1995, PhD thesis, Univ. Groningen
Impey C. D., Malkan M. A., Webb W., Petry C. E., 1995, ApJ, 440, 80
Jeffrey D. J., 1990, ApJ, 352, 267
Koratkar A., Antonucci R. R. J., Bushouse H., Kinney A., 1995, ApJ, 450, 501
Korista K. T., Voit G. M., Morris S. L., Weymann R. J., 1993, ApJS, 88, 357
Laor A., Draine B. T., 1993, ApJ, 402, 441
Laor A., Netzer H., Piran T., 1990, MNRAS, 242, 560
Lee H.-W., 1994, MNRAS, 268, 49 (Paper II)
Lee H.-W., Blandford R. D., Western L., 1994, MNRAS, 267, 303 (Paper I)
Miller J. S., Goodrich R. W., 1990, ApJ, 355, 456
Murray N., Grossman S. A., Chiang J., Voit M., 1995, ApJ, 451, 498
Netzer H., 1990, Active Galactic Nuclei. Springer, Berlin
Osterbrock D. E., 1989, Astrophysics of Gaseous Nebulae and Active Galactic Nuclei. Univ. Science Books, Mill Valley
Perry J., Dyson J. E., 1985, MNRAS, 213, 665
Perry J. J., Williams R., 1993, MNRAS, 260, 437
Peterson B. M., Reichert G. A., Korista K. T., Wagner R. M., 1990, ApJ, 352, 68
Peterson B. M. et al., 1991, ApJ, 368, 119
Peterson B. M. et al., 1994, ApJ, 425, 622
Rauch K. P., Blandford R. D., 1991, ApJ, 381, L39
Rees M. J., 1987, MNRAS, 228, 47P
Rybicki G. B., Hummer D. G., 1978, ApJ, 219, 654
Scoville N., Norman C., 1995, ApJ, 451, 510
Shields J., Ferland G., Peterson B. M., 1995, ApJ, 441, 507
Smith P. S., Schmidt G. D., Allen R. G., Angel J. R. P., 1995, ApJ, 444, 146
Sobolev V. V., 1947, Moving Envelopes of Stars. Leningrad State Univ., Leningrad (English translation: 1960, Gaposchkin S., Harvard Univ. Press, Cambridge, MA)

Stockman H. S., Angel J. R. P., Miley G. K., 1979, ApJ, 227, L55
Stockman H. S., Angel J. R. P., Hier R. G., 1981, ApJ, 243, 404
Tran H. D., Miller J. S., Kay L. E., 1992, ApJ, 397, 452
Turnshek D. A., 1988, in Blades S. C., Turnshek D. A., Norman C. A., eds, Space Telescope Sci. Inst. Symp. 2, QSO Absorption Lines: Probing the Universe. Cambridge Univ. Press, Cambridge, p. 17
Verner D. A., Barthel P. D., Tytler D., 1994, A&AS, 108, 287
Weymann R. J., 1970, ApJ, 160, 31
Weymann R. J., Scott J. S., Schiano A. V. R., Christiansen W. A., 1982, ApJ, 262, 497
Weymann R. J., Turnshek D. A., Christiansen W. A., 1985, in Miller J., ed., Astrophysics of Active Galaxies and Quasi-Stellar Objects. Univ. Science Books, Mill Valley
Weymann R. J., Morris S. L., Foltz C. B., Hewett P. C., 1991, ApJ, 373, 23
Williams R., Perry J. J., 1994, MNRAS, 269, 538
Wilson A. S., 1994, in Ward M. J., ed., Proceedings of the Oxford Torus Workshop. Oxford

APPENDIX A: POLARIZATION SCATTERING MATRIX

In this appendix, we describe how to compute the scattering matrix for scattering of polarized radiation when the radiation field is axisymmetric with respect to the direction $\hat{\boldsymbol{r}}$. We assume radiative mixing of the ground sublevels when $J_g \geq 1$. Let the incident photons be characterized by the wavevector $\boldsymbol{n}_i = (\sin\theta_i \cos\phi_i, \sin\theta_i \sin\phi_i, \cos\theta_i)$ and polarization vector $\boldsymbol{e}^i_\alpha$, where $\alpha = \|, \perp$ are the components parallel and perpendicular to the $\hat{\boldsymbol{r}}$–$\boldsymbol{n}_i$ plane.

Adopting the notation of Paper I, the matrix elements are given by

$$M_{eg}(\boldsymbol{e}^i_\|) = [2^{-1/2} \cos\theta_i e^{i\phi_i} R^{-1}_{eg}, \ -\sin\theta_i R^0_{eg}, \ -2^{-1/2} \cos\theta_i e^{-i\phi_i} R^1_{eg}] \tag{A1}$$

$$M_{eg}(\boldsymbol{e}^i_\perp) = [2^{-1/2} i e^{i\phi_i} R^{-1}_{eg}, \ 0, \ 2^{-1/2} i e^{-i\phi_i} R^1_{eg}].$$

We now expand our basis eigenstates with respect to $\hat{\boldsymbol{r}}$ so that both the ground and excited density matrices will be diagonal and we write the ground state occupation probabilities as ρ_g, $-J_g \leq g \leq J_g$, normalized so that $\sum_g \rho_g = 1$. (Note that $\rho_g = \rho_{-g}$.) In equilibrium, the excited state occupation probabilities are given by

$$\tilde{\rho}_e = \int d\Omega_i \sum_{\alpha g} \mathcal{N}_\alpha M_{eg}(\boldsymbol{e}^i_\alpha) \rho_g M^*_{eg}(\boldsymbol{e}^i_\alpha), \tag{A2}$$

where $d\Omega_i = \sin\theta_i \, d\theta_i \, d\phi_i$ and $\mathcal{N}_\alpha$ is the photon occupation number (assumed $\ll 1$) in the polarization state $\boldsymbol{e}^i_\alpha$. Averaging over azimuth, this becomes

$$\tilde{\rho}_e = \left(\frac{1}{2}\cos^2\theta_i \mathcal{N}_\| + \mathcal{N}_\perp\right) |R^1_{ee-1}|^2 \rho_{e-1} + \sin^2\theta_i \mathcal{N}_\| |R^0_{ee}|^2 \rho_e + \left(\frac{1}{2}\cos^2\theta_i \mathcal{N}_\| + \mathcal{N}_\perp\right) |R^{-1}_{ee+1}|^2 \rho_{e+1}. \tag{A3}$$

The scattered radiation field is given by

$$j_{\alpha\alpha'} = \sum_{e,g} M^*_{eg}(\boldsymbol{e}^o_\alpha) \tilde{\rho}_e M_{eg}(\boldsymbol{e}^o_{\alpha'}), \tag{A4}$$

where the outgoing wavevector is given by $\boldsymbol{n}_o = (\sin\theta_o \cos\phi_o, \sin\theta_o \sin\phi_o, \cos\theta_o)$ and the polarization vectors now refer to the $\hat{\boldsymbol{r}}$–$\boldsymbol{n}_o$ plane. The direct substitution of equation (A3) into equation (A4) and averaging over the azimuth ϕ_o gives

$$\begin{aligned} j_{\|\|} &= \sum_e \left\{\frac{1}{2}\cos^2\theta_o [(R^{-1}_{ee+1})^2 + (R^1_{ee-1})^2] + \sin^2\theta_o (R^0_{ee})^2\right\} \\ &\times \left[\left[\frac{1}{2}(\mathcal{N}_\| \cos^2\theta_i + \mathcal{N}_\perp)\{C_{e+1}(R^{-1}_{ee+1})^2 + C_{e-1}[R^1_{e-1}(R^1_{ee-1})^2\} + \mathcal{N}_\| \sin^2\theta_i C_e (R^0_{ee})^2\right]\right], \end{aligned} \tag{A5}$$

$$\begin{aligned} j_{\perp\perp} &= \sum_e \frac{1}{2}[(R^{-1}_{ee+1})^2 + (R^1_{ee-1})^2] \\ &\times \left\{\frac{1}{2}(\mathcal{N}_\| \cos^2\theta_i + \mathcal{N}_\perp)[C_{e+1}(R^{-1}_{ee+1})^2 + C_{e-1}(R^1_{ee-1})^2] + \mathcal{N}_\| \sin^2\theta_i C_e (R^0_{ee})^2\right\}, \end{aligned}$$

$$j_{\|\perp} = j_{\perp\|} = 0.$$

From equation (A5) we obtain the scattering matrix S, defined by the relation

$$\begin{pmatrix} J_\| \\ J_\perp \end{pmatrix} = S \begin{pmatrix} n_\| \\ n_\perp \end{pmatrix}, \tag{A6}$$

where $J_\| \equiv J_{\|\|}$, and similarly for $J_\perp$.

The elements of S are given by

$$\begin{aligned} S_{\|\|} &= \sum_e \left\{\frac{1}{2}\cos^2\theta_o [(R^{-1}_{ee+1})^2 + (R^1_{ee-1})^2] + \sin^2\theta_o (R^0_{ee})^2\right\} \\ &\times \left\{\frac{1}{2}\cos^2\theta_i [C_{e+1}(R^{-1}_{ee+1})^2 + C_{e-1}(R^1_{ee-1})^2] + \sin^2\theta_i C_e (R^0_{ee})^2\right\}, \end{aligned}$$

$$\begin{aligned} S_{\|\perp} &= \sum_e \left\{\frac{1}{2}\cos^2\theta_o [(R^{-1}_{ee+1})^2 + (R^1_{ee-1})^2] + \sin^2\theta_o (R^0_{ee})^2\right\} \\ &\times \frac{1}{2}[C_{e+1}(R^{-1}_{ee+1})^2 + C_{e-1}(R^1_{ee-1})^2], \end{aligned} \tag{A7}$$

$$\begin{aligned} S_{\perp\|} &= \sum_e \frac{1}{2}[(R^{-1}_{ee+1})^2 + (R^1_{ee-1})^2] \\ &\times \left\{\frac{1}{2}\cos^2\theta_i [C_{e+1}(R^{-1}_{ee+1})^2 + C_{e-1}(R^1_{ee-1})^2] + \sin^2\theta_i C_e (R^0_{ee})^2\right\}, \end{aligned}$$

$$S_{\perp\perp}=\sum_e \frac{1}{2}[(R^{-1}_{ee+1})^2+(R^{1}_{ee-1})^2]$$

$$\times\frac{1}{2}[C_{e+1}(R^{-1}_{ee+1})^2+C_{e-1}(R^{1}_{ee-1})^2].$$

Noting the relations

$$(R^{-1}_{ee+1})^2=(R^{1}_{-e-e-1})^2 \tag{A8}$$

$$(R^{0}_{ee})^2=(R^{0}_{-e-e})^2, \tag{A9}$$

we obtain simpler relations

$$S_{\parallel\parallel}=\sum_e\left\{\frac{1}{2}\cos^2\theta_o[(R^{-1}_{ee+1})^2+(R^{1}_{ee-1})^2]+\sin^2\theta_o(R^{0}_{ee})^2\right\}$$

$$\times[\cos^2\theta_i C_{e+1}(R^{-1}_{ee+1})^2+\sin^2\theta_i C_e(R^{0}_{ee})^2]$$

$$S_{\parallel\perp}=\sum_e\left\{\frac{1}{2}\cos^2\theta_o[(R^{-1}_{ee+1})^2+(R^{1}_{ee-1})^2]+\sin^2\theta_o(R^{0}_{ee})^2\right\}$$

$$\times C_{e+1}(R^{-1}_{ee+1})^2 \tag{A10}$$

$$S_{\perp\parallel}=\sum_e\frac{1}{2}[(R^{-1}_{ee+1})^2+(R^{1}_{ee-1})^2]$$

$$\times[\cos^2\theta_i C_{e+1}(R^{-1}_{ee+1})^2+\sin^2\theta_i C_e(R^{0}_{ee})^2]$$

$$S_{\perp\perp}=\sum_e\frac{1}{2}[(R^{-1}_{ee+1})^2+(R^{1}_{ee-1})^2]\times C_{e+1}(R^{-1}_{ee+1})^2$$

The population of the ground state sublevels after the scattering is given by

$$\tilde{\rho}'_g=\sum_e\tilde{\rho}_e M^*_{eg}(\boldsymbol{e}^o_\alpha)M_{eg}(\boldsymbol{e}^o_{\alpha'})$$

$$=\frac{1}{2}(\cos^2\theta_o+1)[(R^{1}_{g+1g})^2\tilde{\rho}_{g+1}+(R^{-1}_{g-1g})^2\tilde{\rho}_{g+-1}] \tag{A11}$$

$$+\sin^2\theta_o(R^{0}_{gg})^2\tilde{\rho}_g.$$

APPENDIX B: EQUATORIAL FLOW MODEL

We model an equatorial flow using oblate spheroidal coordinates, referred to a circular disc of radius d,

$$x=d\cosh\mu\sin\lambda\cos\phi$$

$$y=d\cosh\mu\sin\lambda\sin\phi \tag{B1}$$

$$z=d\sinh\mu\cos\lambda,$$

setting $\lambda=$constant along a flow line. For the velocity field, we adopt

$$v_p=\dot{\mu}(\sinh^2\mu+\cos^2\lambda)^{1/2}=A(1/\sin\lambda-1/r^{1/2})$$

$$v_\phi=\dot{\phi}\cosh\mu\sin\lambda\propto 1/\cosh\mu\sin\lambda=B/r\sin\theta. \tag{B2}$$

The equation of a Sobolev surface corresponding to equation (4.4) is given by

$$v_l=d(\dot{\mu}\sinh\mu\sin\lambda\cos\phi-\dot{\phi}\cosh\mu\sin\lambda\sin\phi)\sin\theta_o$$

$$+d_0\dot{\mu}\cosh\mu\cos\lambda\cos\theta_o$$

$$=\left\{\frac{A[r^{1/2}-(d\sin\lambda)^{1/2}]}{[r\sin\lambda(\sinh^2\mu+\cos^2\mathrm{m}\lambda)]^{1/2}}\right\}$$

$$\times(\sinh\mu\sin\lambda\cos\phi\sin\theta_0+\cosh\mu\cos\lambda\cos\theta_0)$$

$$-\frac{B\sin\phi\sin\theta_0}{r\sin\theta}, \tag{B3}$$

where $r=d(\sinh^2\mu+\sin^2\lambda)^{1/2}$.

The conserved number flux corresponding to equation (A5) is

$$N(\lambda)\,\mathrm{d}\lambda=\pi n(\mu,\lambda)d^3\dot{\mu}\cosh\mu\sin\lambda(\sinh^2\mu+\cos^2\lambda)\,\mathrm{d}\lambda \tag{B4}$$

and the density is

$$n(\mu,\lambda)= \tag{B5}$$

$$\frac{(r\sin\lambda)^{1/2}h(\lambda)}{\pi Ad^{3/2}\cosh\mu\sin\lambda(\sinh^2\mu+\cos^2\lambda)^{1/2}[r^{1/2}-(d\sin\lambda)^{1/2}]},$$

where $h(\lambda)$ is a function to be specified.

These relations are sufficient to compute the Sobolev optical depth along a ray.

APPENDIX C: BIPOLAR FLOW MODEL

We model a bipolar outflow using a simple model in which the poloidal velocity lies on level surfaces ($\xi_2=$constant) of the paraboloidal coordinate system in which

$$x=\xi_1\xi_2\cos\phi$$

$$\phi\tau\zeta\theta=\xi_1\xi_2\sin\phi \tag{C1}$$

$$z=\frac{1}{2}(\xi_1^2-\xi_2^2).$$

We adopt simple, kinematic prescriptions for the poloidal and toroidal velocity components describing an accelerating flow in which mechanical angular momentum is conserved:

$$v_p=\dot{\xi}_1(\xi_1^2+\xi_2^2)^{1/2}=A\left[\frac{1}{\xi_2}-\left(\frac{1}{r}\right)^{1/2}\right] \tag{C2}$$

$$v_\phi=\dot{\phi}\xi_1\xi_2=\frac{B}{\xi_1\xi_2},$$

where $r=(\xi_1^2+\xi_2^2)/2$ and A, B are constants.

The equation of a Sobolev surface is given by $\boldsymbol{v}\cdot\hat{\boldsymbol{n}}=v_l=$constant. Making use of the relations

$$\xi_1=(r+z)^{1/2}=r^{1/2}(1+\cos\theta)^{1/2}$$

$$\xi_2=(r-z)^{1/2}=r^{1/2}(1-\cos\theta)^{1/2}, \tag{C3}$$

we obtain

$$v_l=\left(\frac{A}{r^{1/2}}\right)\left[\frac{1-(1-\cos\theta)^{1/2}}{(1-\cos\theta)^{1/2}}\right]$$
$$=[(1+\cos\theta)^{1/2}\cos\phi\sin\theta_o+(1-\cos\theta)^{1/2}\cos\theta_o] \quad \text{(C4)}$$
$$-B\sin\phi\sin\theta_o/r\sin\theta,$$

where $\hat{\boldsymbol{n}}=(\sin\theta_o, 0, \cos\theta_o)$. This can be solved as a quadratic for $r^{1/2}$.

Since ξ_2=constant along a streamline, the number flux across the surface z=constant with ξ_2 in $\mathrm{d}\xi_2$ must be independent of ξ_1 and therefore satisfies

$$N(\xi_2)\,\mathrm{d}\xi_2=n(\xi_1,\xi_2)\dot{\xi}_1\xi_1\xi_2(\xi_1^2+\xi_2^2)\,\mathrm{d}\xi_2. \quad \text{(C5)}$$

Hence

$$n(\xi_1,\xi_2)=$$
$$\sqrt{1-\cos\theta}f(\xi_2)/[\sqrt{2}A_v r\sin\theta(1-\sqrt{1-\cos\theta})], \quad \text{(C6)}$$

where $f(\xi_2)$ is a function to be specified.